Processing and Application of Ceramics 19 [4] (2025) 334–351
https://doi.org/10.2298/PAC2504334L

A novel high-entropy $(Sc_{0.2}La_{0.2}Sm_{0.2}Er_{0.2}Yb_{0.2})_2Zr_2O_7$ ceramics with excellent thermophysical properties designed by thermal properties tailoring theory

Jiahang Liu[1], Yiyong Wang[1], Zhe Lu[1,*], Yeon-Gil Jung[3,*], Yanwen Zhou[1], Yan Li[3], Honglin Guo[1]

[1] *School of Materials & Metallurgy, University of Science and Technology Liaoning, Anshan 114051, China*
[2] *School of Materials Science and Engineering, Changwon National University Changwon, Gyeongnam 51140, Korea*
[3] *Tangshan Shoutang Baosheng Function Materials Co. Ltd, Tangshan 063110, China*

Received 29 September 2025; Received in revised form 20 November 2025; Accepted 27 November 2025

Abstract

The outstanding thermophysical properties and mechanical properties are crucial for the application of $RE_2Zr_2O_7$ in thermal barrier coatings (TBCs). To simultaneously optimize the thermal conductivity, thermal expansion behaviour and mechanical properties of rare-earth zirconate ceramics, in this work a novel high-entropy $(Sc_{0.2}La_{0.2}Sm_{0.2}Er_{0.2}Yb_{0.2})_2Zr_2O_7$ (REZO) ceramics was designed with significant mass and size differences based on the thermal properties tailoring theory. Structural analysis revealed that the REZO ceramics prepared by conventional solid-state reaction exhibits a dual-phase structure with coexisting pyrochlore and fluorite phases, and the five rare-earth cations were uniformly distributed throughout REZO without compositional segregation. In terms of thermophysical properties, compared to $La_2Zr_2O_7$ and $Gd_2Zr_2O_7$, the REZO exhibits a glass-like thermal conductivity ($1.31\,W\cdot m^{-1}\cdot K^{-1}$, at room temperature) and a high thermal expansion coefficient ($11.054 \times 10^{-6}/K$, 1200 °C). Additionally, the REZO demonstrates excellent high-temperature phase stability from room temperature to 1600 °C. In terms of mechanical properties, the REZO exhibits a lower Young's modulus, higher Vickers hardness and higher fracture toughness compared to $La_2Zr_2O_7$ and $Gd_2Zr_2O_7$. In summary, the thermal properties tailoring theory employed in this work provides a novel design approach for developing $RE_2Zr_2O_7$ ceramics with tunable thermophysical and mechanical properties, enhancing the application prospects of $RE_2Zr_2O_7$ in advanced TBCs.

Keywords: *high-entropy $RE_2Zr_2O_7$, thermal barrier coating, thermophysical and mechanical properties*

I. Introduction

In the heavy industry sector, heavy-duty gas turbines are the most common equipment used for converting thermal energy into power [1]. Heavy-duty gas turbines use oil or natural gas as a fuel, driving turbine equipment and providing power through the high-temperature gases generated during combustion [2]. In recent years, the demands for energy conservation and environmental protection have increased, driving higher performance requirements for heavy-duty gas turbines and toward the targets of high efficiency and low emissions [3]. Two primary factors influence gas turbine efficiency, including turbine inlet temperature and compressor compression ratio. Among them, increasing the turbine inlet temperature is crucial for thermal efficiency and gas turbine performance [4]. Therefore, as the core component of gas turbines, enhancing turbine inlet temperature primarily relies on three approaches: developing high-temperature-resistant metallic materials, designing advanced cooling structures and utilizing thermal barrier coating technology [5–7]. Compared to the other two methods, thermal barrier coating technology offers lower costs and superior thermal insulation performance. It has been demonstrated that apply-

---

[*] Corresponding author:
e-mail: *lz19870522@126.com* (Zhe Lu)
jungyg@changwon.ac.kr (Yeon-Gil Jung)

ing a 100–500 μm thermal barrier coating on the turbine blade surface via thermal spraying prevents direct contact between high-temperature combustion gases and the blades, reducing surface temperatures by approximately 100–300 °C [8]. This enables the safe operation of heavy-duty gas turbines. As the most widely used thermal barrier coating material in engineering applications, 6–8 wt.% yttria-stabilized zirconia (YSZ) exhibits outstanding mechanical properties, with the hardness and elastic modulus of approximately 10 and 220 GPa, respectively [9]. However, YSZ coatings undergo phase transformation and sintering above 1200 °C, leading to inhomogeneous internal stresses and reduction of the service life of the thermal barrier coating [10]. To enable long-term operation of thermal barrier coatings at temperatures exceeding 1200 °C, the development of novel ceramic materials is essential.

In recent years, researchers have developed a series of novel thermal barrier coating materials by leveraging the advantages of materials chemistry and rare-earth chemistry, such as rare-earth zirconates ($RE_2Zr_2O_7$) [11], rare-earth cerates ($RE_2Ce_2O_7$) [12], rare-earth stannates ($RE_2Sn_2O_7$) [13] and rare-earth tantalates ($RETaO_4$) [14]. Among them, $RE_2Zr_2O_7$ exhibit a significant phonon scattering due to the complex crystal structure and inherent 1/8 oxygen vacancy, resulting in a thermal conductivity approximately 30% lower than that of YSZ [15]. However, currently applied $RE_2Zr_2O_7$ compounds still exhibit certain limitations. For instance, the thermal expansion coefficient (TEC) of $La_2Zr_2O_7$ (LZO) at the high-temperature range is significantly lower than that of 8YSZ [16]. Therefore, optimizing the comprehensive properties of $RE_2Zr_2O_7$ to satisfy the requirements of advanced thermal barrier coatings is necessary. Currently, doping modification has been widely applied to optimize the properties of $RE_2Zr_2O_7$. For example, Xu *et al.* [17] prepared $(Y_{0.05}La_{0.95})_2(Zr_{0.7}Ce_{0.3})_2O_7$ ceramics by the solid-state reaction method, introducing Ce–O and Y–O bonds with lower bonding energy in $La_2Zr_2O_7$ to make its TEC reach $10.58 \times 10^{-6}\,K^{-1}$, which is 1.15 times that of the conventional $La_2Zr_2O_7$. Wang *et al.* [18] investigated the effect of Hf^{4+} substitution at the Zr^{4+} site in $La_2Zr_2O_7$ on thermal conductivity, concluding that introduction of the large-sized substitution atoms into the $La_2(Zr_{1-x}Hf_x)_2O_7$ ($0 \leq x \leq 0.5$) system represents a viable approach to significantly reduce thermal conductivity.

The concept of "high-entropy" and its application to the design and preparation of alloy materials was proposed in 2004 [19,20]. High-entropy materials are solid solutions composed of five or more elements, providing numerous combinatorial options that enhance performance and allow for customized design. In 2015, Rost *et al.* [21] successfully synthesized high-entropy oxide ceramics with uniform element distribution and a single structure using five oxides of MgO, NiO, CoO, CuO and ZnO as raw materials, which successfully introduced the "high-entropy" concept into the ceramics field. In current research, high-entropy ceramics play a significant role due to the novelty of the composition. The interactions between different components and their tunable properties have also attracted considerable attention [22]. Among them, high-entropy $RE_2Zr_2O_7$ (HE-$RE_2Zr_2O_7$) containing five or more rare-earth cations exhibits four core effects, including the high-entropy effect, severe-lattice-distortion effect, sluggish diffusion effect and "cocktail" effect [23]. These characteristics enable HE-$RE_2Zr_2O_7$ to show distinct thermal and mechanical properties compared to the single-component $RE_2Zr_2O_7$ offering a capability of further modulation of relevant properties through composition adjustments [24]. For instance, Luo *et al.* [25] synthesized a five-component HE-$RE_2Zr_2O_7$ containing Dy, Nd, Sm, Eu and Yb, and this material exhibited outstanding sintering resistance under high-temperature conditions. Furthermore, its fracture toughness reached $2.07 \pm 0.03\,MPa\cdot m^{1/2}$, which is 1.5 times that of $La_2Zr_2O_7$. Zhao *et al.* [26] designed a novel high-entropy $RE_2Zr_2O_7$ by simultaneously introducing elements with different valence states, namely $(La_{0.3}Gd_{0.3}Ca_{0.4})_2(Ti_{0.2}Zr_{0.2}Hf_{0.2}Ta_{0.2})_2O_7$. Due to the significant radius difference and mass difference, the thermal conductivity of this ceramics at room temperature is only $1.56\,W\cdot m^{-1}\cdot K^{-1}$, lower than that of traditional $La_2Zr_2O_7$ ($2.21\,W\cdot m^{-1}\cdot K^{-1}$). Fan *et al.* [27] designed a $(Y_{0.2}Gd_{0.2}Er_{0.2}Yb_{0.2}Lu_{0.2})_2Zr_2O_7$ high-entropy ceramics with excellent CMAS corrosion resistance in a high-temperature environment. By optimizing the chemical stability and high-entropy effect, the CMAS corrosion depth at 1300 °C was 22.6% of $Gd_2Zr_2O_7$ (GZO) and 2.6% of YSZ. In summary, the benefit of high-entropy modification is that it can enhance the overall properties of HE-$RE_2Zr_2O_7$ and achieve targeted performance improvements through doping with various elements.

An important technical advantage of high-entropy modification for $RE_2Zr_2O_7$ ceramics is the extensive flexibility in the compositional design and controllable comprehensive properties. This has resulted in a vast composition database and various performance characteristics for HE-$RE_2Zr_2O_7$, making it challenging to experimentally verify the properties of different materials individually. In addition, current reports on HE-$RE_2Zr_2O_7$ often ignore the impact of radius and mass differences on the performance. Although several new high-entropy material systems have been synthesized, research on composition design and performance characterization based on the performance influence mechanisms of high-entropy ceramics and thermophysical property design principles remains relatively scarce. Therefore, based on the thermal properties tailoring theory of HE-$RE_2Zr_2O_7$, in this work a high-entropy $(Sc_{0.2}La_{0.2}Sm_{0.2}Er_{0.2}Yb_{0.2})_2Zr_2O_7$ (REZO) ceramics was designed by utilizing the phonon scattering mechanism and the relationship between thermal expansion and electronegativity difference. This work systematically investigates the phase composition, crystal structure, thermophysical and mechanical properties of REZO. It also highlights the fundamental principles of thermophysical property design for achieving composition optimization and performance modification in HE-$RE_2Zr_2O_7$, enabling the tailored adjustment of thermal barrier coating properties to meet specific requirements.

II. Experimental

2.1. Material design

Thermal conductivity and thermal expansion coefficient are the two most critical thermophysical properties of thermal barrier coating materials, which directly impact the high-temperature service life of both the metallic substrate and thermal barrier coatings [28]. Among them, the lower thermal conductivity can reduce the heat flow density within the coating, resulting in a decrease in the surface temperature of the metallic substrate. According to the kinetic theory of heat conduction, the phonon mean free path is a key factor determining a material's thermal conductivity, and the thermal conductivity of ceramic materials decreases as the phonon mean free path reduces [29]. Based on the perturbation theory, the phonon mean free path (l) is negatively correlated with the mass difference ($\Delta M/M$) and the radius difference ($\Delta R/R$), as expressed by the following equations [30]:

$$\frac{1}{l} = \frac{c\alpha^3\omega^4}{4\pi v^4}\left(\frac{\Delta M}{M}\right)^2 \tag{1}$$

$$\frac{1}{l} = \frac{2c\alpha^3\omega^4}{4\pi v^4}J^4\gamma^4\left(\frac{\Delta R}{R}\right)^2 \tag{2}$$

where α^3, v, ω, c, J, γ, M and R represent the atomic volume per unit cell, transverse wave velocity, phonon frequency, atomic defect concentration per unit cell, a constant, Gruneisen parameter, average atomic mass and average ionic radius, respectively. Based on the substitution sites of rare-earth cations in HE-$RE_2Zr_2O_7$, $\Delta M/M$ and $\Delta R/R$ can be calculated by [31]:

$$\frac{\Delta M}{M} = \frac{\sqrt{\sum_{i=1}^{n} c_i(M_i - \sum_{i=1}^{n} c_i M_i)^2}}{\sum_{i=1}^{n} c_i M_i} \tag{3}$$

$$\frac{\Delta R}{R} = \frac{\sqrt{\sum_{i=1}^{n} c_i(R_i - \sum_{i=1}^{n} c_i R_i)^2}}{\sum_{i=1}^{n} c_i R_i} \tag{4}$$

where n is the atom number, c_i, M_i and R_i represent the molar content, atomic mass, and ionic radius of the i-th element, respectively. Therefore, theoretically, thermal conductivity reduction can be achieved by selecting rare-earth cations with significant differences in atomic mass and Shannon ionic radius for doping. In this work, rare-earth elements were selected for high-entropy modification. Sc^{3+} and Yb^{3+}, exhibiting significant differences in atomic mass, were chosen as two cations to ensure substantial mass differences. Due to the significant difference in Shannon ionic radius between La^{3+} and Sc^{3+}, La^{3+} was selected to increase the size difference within high-entropy ceramics. In addition, Sm^{3+} and Er^{3+} were selected to increase the configuration entropy of $RE_2Zr_2O_7$. Table 1 lists the intrinsic properties of different elements. Accordingly, the $\Delta M/M$ and $\Delta R/R$ values of $(Sc_{0.2}La_{0.2}Sm_{0.2}Er_{0.2}Yb_{0.2})_2Zr_2O_7$ designed in this work were 1.022 and 0.229, respectively, which are higher than those of $La_2Zr_2O_7$ ($\Delta M/M$ = 0.956, $\Delta R/R$ = 0.209) and $Gd_2Zr_2O_7$ ($\Delta M/M$ = 1.006, $\Delta R/R$ = 0.219) (as shown in Table 2).

In terms of thermal expansion coefficient, the higher thermal expansion coefficient of ceramic materials can reduce thermal stress within the coating system and slow down the formation and propagation of cracks [32]. According to the relevant theory of thermal expansion, the thermal expansion coefficient of a material is negatively correlated with the ionic bond strength, and the ionic bond strength is positively correlated with the average electronegativity of cations and anions [33]. Therefore, by selecting rare-earth cations with different electronegativities for doping, the thermal expansion coefficient can be adjusted. The ionic bond strength between cation RE and anion O (I_{RE-O}) can be esti-

Table 1. Oxidation state, coordination number, electronegativity (χ_i), atomic mass (M_i) and Shannon ionic radius (R_i) of different elements

Elements	Sc	La	Sm	Er	Yb	Zr	O
Oxidation state	3	3	3	3	3	4	-2
Coordination number	VIII	VIII	VIII	VIII	VIII	VI	VI
Atomic mass, M_i	44.9	138.9	150.4	167.2	173	91.2	16
Electronegativity, χ_i	1.36	1.1	1.17	1.24	1.1	1.33	3.44
Shannon ionic radius [Å]	0.87	1.16	1.079	1.004	0.985	0.72	1.40

Table 2. Composition, average radius (r_{RE}), cation radius ratio (r_{RE}/r_{Zr}), size disorder (δ), mass difference ($\Delta M/M$), radius difference ($\Delta R/R$) and ionic bond strength between cation RE and anion O (I_{RE-O})

Composition		r_{RE} [Å]	r_{RE}/r_{Zr}	δ [%]	$\Delta M/M$	$\Delta R/R$	I_{RE-O}
$La_2Zr_2O_7$	LZO	1.16	1.611	0	0.956	0.209	0.709
$Gd_2Zr_2O_7$	GZO	1.053	1.462	0	1.006	0.219	0.695
$(Sc_{0.2}La_{0.2}Sm_{0.2}Er_{0.2}Yb_{0.2})_2Zr_2O_7$	REZO	1.019	1.416	9.559	1.021	0.229	0.698

mated by the Pauling electronegativity empirical equation [34]:

$$I_{\text{RE-O}} = 1 - \exp\left(\frac{(\chi_0 - \chi_{avg})^2}{4}\right) \tag{5}$$

$$\chi_{avg} = \sum_{i=1}^{n} c_i \chi_i \tag{6}$$

where n is the number of atoms, c_i and χ_i represent the atomic friction and electronegativity of the i-th element, respectively. χ_{avg} represents the average electronegativity. As shown in Table 2, the $I_{\text{RE-O}}$ value of $(Sc_{0.2}La_{0.2}Sm_{0.2}Er_{0.2}Yb_{0.2})_2Zr_2O_7$ is 0.698, which is lower than that of $La_2Zr_2O_7$ (0.709) and close to $Gd_2Zr_2O_7$ (0.695).

2.2. *Sample preparation*

Dense REZO ceramics was synthesized by a conventional solid-state reaction. The raw powders used were commercially available microsize Sc_2O_3, La_2O_3, Sm_2O_3, Er_2O_3, Yb_2O_3 and ZrO_2 (99.9% purity, Shanghai Yaotian nano, Co. Ltd, China, average particle size: 1 µm). Before weighing, all powders were calcined at 900 °C for 4 h to remove moisture and impurities. The calcined powders were precisely weighted according to the theoretical chemical composition, and the weighted raw materials were placed into ZrO_2 ball milling jars. A planetary ball mill was employed for wet mixing, utilizing ZrO_2 balls as grinding media and anhydrous ethanol as the solvent. A mass ratio of 5:1 between ZrO_2 balls and raw powder was maintained. The ball milling speed was set at 400 rpm, with a grinding period of 48 h. The homogeneously mixed ceramic slurry was placed in a drying oven at 80 °C for 48 h. Then the dried ceramic powder mixture was sieved through a 300-mesh screen. The powder was pressed into ceramic green bodies using an electric tablet press machine at 100 MPa with 10 min holding time. The ceramic green bodies were then placed in a cold isostatic press and subjected to cold isostatic pressing at a pressure of 250 MPa with a holding time of 5 min. After pressing, the green bodies were removed and stored at room temperature for 24 h to release internal stresses. Finally, the ceramic green bodies were placed in a muffle furnace and heated with a heating rate of 10 °C/min to 1600 °C. After holding at 160 °C for 24 h, the ceramic samples were naturally cooled in the furnace to room temperature. For comparison, dense $La_2Zr_2O_7$ and $Gd_2Zr_2O_7$ ceramic samples were synthesized using the same process as REZO.

2.3. *Material design characterization*

Phase composition of the ceramic samples was characterized by X-ray diffraction (XRD, D8 advance, Germany) using Cu Kα radiation with a scanning rate of 2 °/min. The diffraction angle scanning interval was set as 2θ = 10–80°. The crystal structure parameter was determined using the Rietveld refinement method with the GSAS software, and the accuracy of the refinement results was evaluated by the R_p and R_{wp}. VESTA software was used to perform the modelling of the pyrochlore structure and the fluorite structure. Since the Raman spectroscopy is sensitive to structural distortions, the Raman spectra of the ceramic samples were collected using a Raman microscope (WITec alpha300 R, Germany) with a laser source of 532 nm. The X-ray photo-electron spectroscopy (XPS, PHI 5000 Versaprobe III, Japan) was used to determine the valence state and oxygen vacancies. The nanostructure and elemental distribution of the ceramic samples were further characterized using transmission electron microscopy (TEM, JEM-F200, Japan). Before the TEM testing, the ceramic samples needed to be milled using the high-energy ball milling method (LPB-2L, Hunan LAISDA Instrument Equipment Co. Ltd, China), and the milled powder was dispersed in anhydrous ethanol and prepared using a Cu mesh. A scanning electron microscope (SEM, ZEISS Sigma 360, Germany) with energy dispersive spectroscopy (EDS, X-MAX20, UK) was used to characterize the sintered samples' surface morphology and elemental distribution. Experimental density (ρ) of the ceramic samples was measured by the Archimedes method, the theoretical density (ρ_0) was calculated based on the refined crystal structure parameters and the relative density (ρ_r) was calculated as follows [35]:

$$\rho_r = \frac{\rho}{\rho_0} \times 100 \tag{7}$$

The Vickers hardness (H_V) of the sintered samples was obtained using a Vickers microhardness tester (Qness 60 A+ EVO) under a 1 kg load for 15 s. Each sample was measured 15 times for Vickers hardness, and the average value was calculated. Fracture toughness was calculated from the indentation morphology of the Vickers hardness, which is as follows [36]:

$$K_{IC} = 0.16 H_V a^2 c^{-\frac{3}{2}} \tag{8}$$

where a is the half-length of the indent diagonal and c is the half-length of the crack obtained from the centre of the indentation to the tip of the crack. The Young's modulus of the sintered samples was measured using an ultrasonic reflection method (UMS-100, Teclab, France). The transverse (V_T) and longitudinal (V_L) acoustic velocities were tested using 5 MHz and 20 MHz probes, respectively. The mean velocity (V_m) and Young's modulus (E) were calculated by [37]:

$$V_M = \left[\frac{1}{3}\left(\frac{1}{V_L^3} + \frac{2}{V_T^3}\right)\right]^{-\frac{1}{3}} \tag{9}$$

$$E = \frac{\rho V_T^2 (3V_L^2 - 4V_T^2)}{V_L^2 - V_T^2} \tag{10}$$

The specific heat capacity (C_p) of the ceramic samples was calculated using the Neumann-Kopp rule [38].

The thermal diffusivity (λ) was measured using a laser flash analyser (LFA 457, Netzsch, Germany) from room temperature to 1000 °C under air conditions. The thermal conductivity (k) was calculated as follows [39]:

$$k = C_p \rho_0 \lambda \tag{11}$$

Due to the presence of porosity (ψ) within the sintered samples, the effect of porosity on thermal conductivity must be considered. The modified thermal conductivity (k') of dense samples was corrected according to Eq. 12 [40]:

$$\frac{k}{k'} = 1 - \frac{4}{3}\psi \tag{12}$$

The thermal expansion rate of the ceramic samples was measured by a thermal dilatometer (DIL 402, Netzsch, Germany) from 100–1200 °C with a heating rate of 5 °C/min, the dimensions of the samples were $4 \times 4 \times 24\,\text{mm}^3$. The relationship between the engineering thermal expansion coefficient and temperature was calculated using Eq. 13 [26]:

$$\alpha = \frac{\mathrm{d}L/L_0}{\mathrm{d}T} \tag{13}$$

where L_0 was the length of the sintered sample at room temperature, dL was the change in the sample length relative to L_0 during testing, and dT was the difference between the test temperature and room temperature.

The high-temperature phase stability of the REZO samples was examined from room temperature to 1500 °C using a synchronous thermal analyser (TG-DSC, Netzsch STA 449 F3 Jupiter, Germany) with a heating rate of 10 °C/min. To detect the phase stability of ceramic materials during long service time in a high-temperature environment, the REZO samples were calcined at 1600 °C for 50, 100 and 150 h, respectively, and the phase composition after calcination was characterized using XRD and Raman spectroscopy.

III. Results and discussion

3.1. Phase composition and microstructure

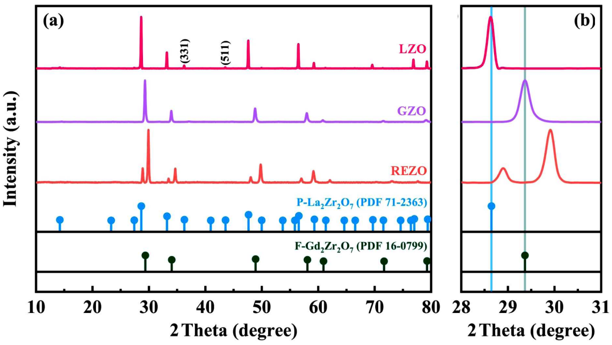

Figure 1. XRD patterns of LZO, GZO, REZO and the standard PDF cards of $La_2Zr_2O_7$ and $Gd_2Zr_2O_7$ (a) and magnified XRD patterns in the 2θ = 28–31° range (b)

Figure 1 presents XRD patterns of three ceramic samples and compares them with the standard PDF cards of $La_2Zr_2O_7$ and $Gd_2Zr_2O_7$. In the XRD patterns of $RE_2Zr_2O_7$, the characteristic peaks from planes (331) and (511) at $2\theta \approx 36.3°$ and 44.3° are the key criteria for distinguishing between the pyrochlore and fluorite structures [41]. In Fig. 1a, the XRD pattern of $La_2Zr_2O_7$ exhibits the diffraction peaks at $2\theta = 36.24°$ and 43.50°, respectively, confirming the pyrochlore structure. In contrast, the XRD pattern of $Gd_2Zr_2O_7$ without peaks from (331) and (511) planes demonstrates its fluorite structure. Remarkably, the diffraction peaks of the REZO are separated into two different groups, corresponding to the standard PDF cards of $La_2Zr_2O_7$ and $Gd_2Zr_2O_7$, respectively, confirming the coexistence of pyrochlore and fluorite structures. According to the existing research, the ratio of cation radius (r_{RE}/r_{Zr}) is the critical factor influencing the crystal structure of single-phase $RE_2Zr_2O_7$ [42]. The $RE_2Zr_2O_7$ tends to form a pyrochlore structure when the r_{RE}/r_{Zr} ratio is in the range of 1.46 to 1.78. Conversely, $RE_2Zr_2O_7$ typically exhibits a fluorite structure when r_{RE}/r_{Zr} is less than 1.46. In this work, the r_{RE}/r_{Zr} of $La_2Zr_2O_7$ and $Gd_2Zr_2O_7$ are 1.611 and 1.462, respectively, indicating that $La_2Zr_2O_7$ exhibits a pyrochlore structure. For $Gd_2Zr_2O_7$, its r_{RE}/r_{Zr} approaches the critical radius at the boundary between the pyrochlore and fluorite structures, which prevents the transition from disordered to ordered structure during cooling. The formation of the dual-phase $RE_2Zr_2O_7$ requires additional consideration of the effect of size disorder (δ), which can be calculated as follows [43]:

$$\delta = \sqrt{\sum_{i=1}^{N} X_i \left(1 - \frac{r_i}{\sum_{i=1}^{N} X_i r_i}\right)^2} \times 100\% \tag{14}$$

where N represents the total number of rare-earth cations, X_i and r_i represent the molar fraction and the Shannon ionic radius of the i-th element, respectively. Fan *et al.* [44] designed various $RE_2Zr_2O_7$ ceramics based on Shannon ionic radius and found that $RE_2Zr_2O_7$ preferred to form a dual-phase structure when r_{RE}/r_{Zr} is within the range of 1.4–1.5 and $\delta > 5.2\%$. In this work, the r_{RE}/r_{Zr} and δ of the REZO sample are 1.416 and 9.515%, respectively. Therefore, the larger size disorder makes REZO to have dual-phase structure.

Figure 1b presents an enlarged view of the diffraction peaks within the 2θ range of 28–31°. Compared with the 222 peak of $La_2Zr_2O_7$ and the 111 peak of $Gd_2Zr_2O_7$, both peaks from (222) and (111) planes of the REZO exhibit a shift toward higher angles. Based on the Bragg diffraction equation $2d \sin\theta = \lambda$, the diffraction peaks shift toward higher angles indicating a decrease in lattice constant. This suggests that smaller rare-earth cations have substituted for the larger La^{3+} and Gd^{3+} ions, respectively, resulting in the formation of a solid solution with a cubic structure.

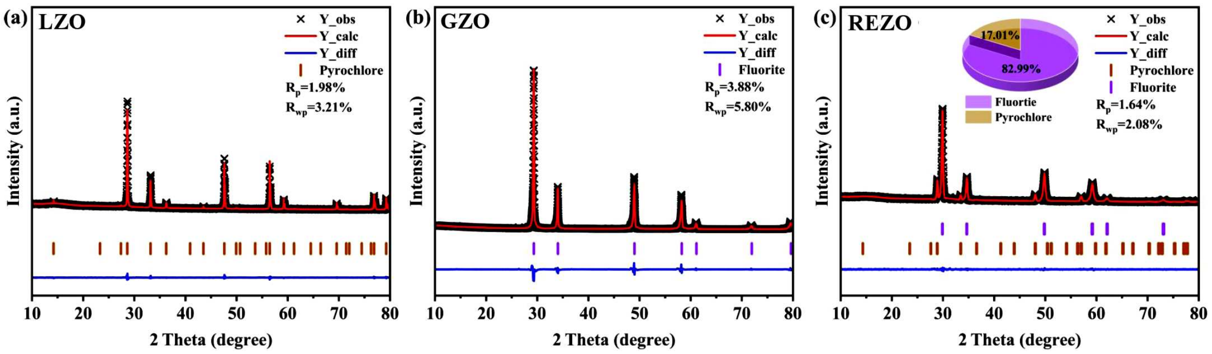

Figure 2. XRD Rietveld refinement patterns of: a) LZO, b) GZO and c) REZO

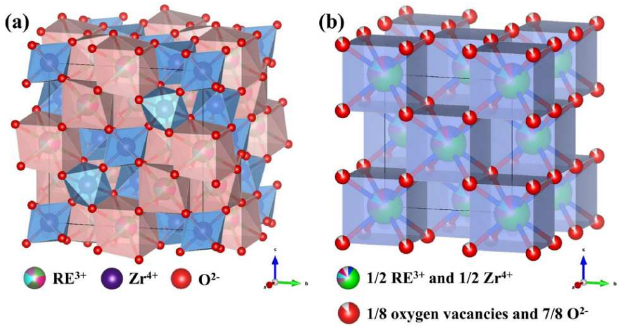

Figure 3. Crystal structure diagram of: a) pyrochlore and b) fluorite

The Rietveld refinement of XRD patterns for LZO, GZO and REZO was carried out using GSAS II software, as shown in Fig. 2. The R_{wp} values of LZO, GZO and REZO were 3.21%, 5.80% and 2.08%, respectively. The R_p values of LZO, GZO and REZO were 1.98%, 3.88% and 1.64%, respectively, indicating that the refinement results are reliable. Table 3 lists the crystal structure, atomic positions, and lattice parameters of the three materials after refinement. In terms of crystal structure, LZO and GZO exhibit a single-phase pyrochlore structure with the $Fd\bar{3}m$ space group and a single-phase fluorite structure with the $Fm\bar{3}m$ space group, respectively. The REZO sample has a dual-phase structure with $Fd\bar{3}m$ pyrochlore structure and $Fm\bar{3}m$ fluorite structure co-existing, which are shown in Fig. 3. In the pyrochlore structure, five types of rare-earth cations randomly occupy the 16*d* (1/2 1/2 1/2) sites and are coordinated by eight O^{2-}; Zr^{4+} occupies the 16*c* (0 0 0) position and coordinates with six O^{2-} to form a $[ZrO_6]$ octahedron [45]. Additionally, the pyrochlore structure contains three distinct oxygen lattice sites. The *x*-value of the O_{48f} is termed the oxygen parameter, and the magnitude of this *x*-value determines the disorder in the pyrochlore structure [18]. The O_{8b} coordinates with four rare-earth ions. The O_{8a} represents an oxygen vacancy, located within a tetrahedron formed by four Zr^{4+} ions. In the fluorite structure, rare-earth cations and Zr^{4+} are randomly distributed at the 4*a* sites, and one intrinsic oxygen vacancy is randomly distributed among every eight 8*c* oxygen sites. In terms of the atomic position, the *x*-value of the O_{48f} in the REZO is 0.3562, higher than that of the LZO (0.3314), indicating severe structure disorder in the REZO. In terms of the lattice parameter, the lattice of fluorite (5.2431 Å) and pyrochlore (10.6417 Å) in the REZO decreased compared with $Gd_2Zr_2O_7$ (5.2631 Å) and $La_2Zr_2O_7$ (10.8066 Å),

Table 3. The structure information of LZO, GZO and REZO

Compounds	$a = b = c$ [Å], $\alpha = \beta = \gamma = 90°$									
	Space group	Atom	x	y	z	*Wyck.*	s.o.f.	a [Å]	V [Å^3]	ρ [g/cm^3]
LZO	$Fd\bar{3}m$	La1	0.5	0.5	0.5	16*d*	1	10.8066	1262.041	6.03
		Zr2	0	0	0	16*c*	1			
		O3	0.3314	0.125	0.125	48*f*	1			
		O4	0.375	0.375	0.375	8*b*	1			
GZO	$Fm\bar{3}m$	Gd1	0	0	0	4*a*	0.5	5.2631	145.789	6.75
		Zr2	0	0	0	4*a*	0.5			
		O3	0.25	0.25	0.25	8*c*	0.875			
REZO	$Fd\bar{3}m$	RE1	0.5	0.5	0.5	16*d*	1	10.6147	1159.978	6.85
		Zr2	0	0	0	16*c*	1			
		O3	0.3562	0.125	0.125	48*f*	1			
		O4	0.375	0.375	0.375	8*b*	1			
	$Fm\bar{3}m$	RE1	0	0	0	4*a*	0.5	5.2431	144.133	
		Zr2	0	0	0	4*a*	0.5			

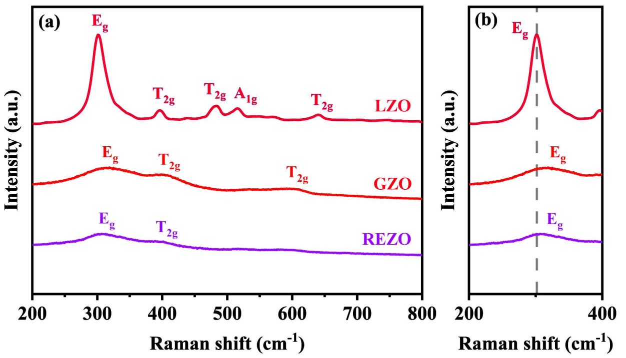

Figure 4. The Raman spectra of LZO, GZO and REZO

respectively. It is noteworthy that the lattice parameters of pyrochlore and fluorite structures in the REZO exhibit significant differences. This difference can be attributed to the unique characteristics of the pyrochlore phase unit cell, which is equivalent to eight fluorite unit cells [41].

Since Raman spectroscopy is more sensitive to structural information and anion disorder, it was performed on the three ceramics at room temperature using a 532 nm laser as the excitation light, and the results are shown in Fig. 4. Based on the group theory analysis, the Raman spectrum of the pyrochlore structure with space group $Fd\bar{3}m$ exhibits six Raman vibration modes, and the Raman spectrum of the fluorite structure with space group $Fm\bar{3}m$ exhibits one Raman vibration mode, which can be expressed as [46]:

$$\Gamma_P = A_{1g} + E_g + 4T_{2g} \tag{15}$$

$$\Gamma_F = T_{2g} \tag{16}$$

The $RE_2Zr_2O_7$-type ceramics with pyrochlore structure can be rewritten as $A_2B_2O_6O'$, where the vibrational modes associated with O_{48f} correspond to A_{1g} + E_g + $3T_{2g}$, while the vibrational mode associated with O_{8a} is T_{2g} [47]. Specifically, the A_{1g} mode primarily relates to O–B–O bending vibrations, the E_g mode mainly corresponds to B–O stretching vibrations, while the T_{2g} mode reflects the combined effects of $B-O_6$ bending, A–O bending/stretching, O–B–O bending, and B–O

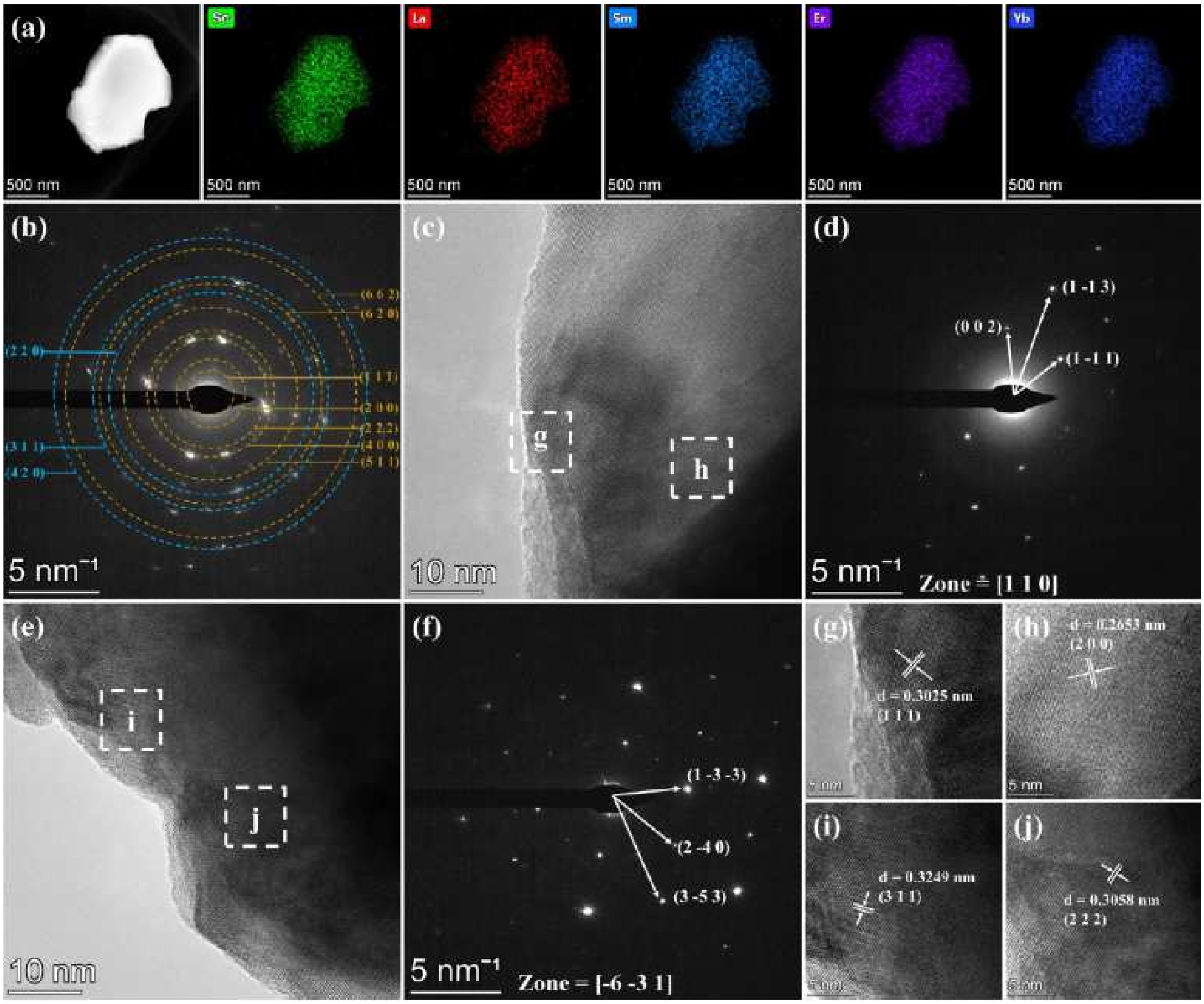

Figure 5. TEM results of REZO: (a) HAADF image and the corresponding EDS mapping, (b) SAED pattern result, (c,e) HRTEM of fluorite and pyrochlore structure, (d,f) SAED of fluorite and pyrochlore structure, and (g-j) magnified images of the region g-j in (c,e)

stretching vibrations. As shown in Fig. 4, LZO exhibits five vibrational modes in the 200–800 cm^{-1} range, displaying distinct Raman vibrational modes characteristic of the pyrochlore structure. The Raman spectrum of GZO exhibits two characteristic peaks ($E_g + T_{2g}$). According to the report of Jafar *et al.* [48], the A_{1g} and E_g characteristic peaks represent the degree of structural order in $RE_2Zr_2O_7$-type ceramic materials. However, the absence of the A_{1g} mode together with the reduced intensity and broadening of the E_g characteristic peak indicates a high degree of structural disorder in GZO. Furthermore, the absence and reduced intensity of the T_{2g} characteristic peak are associated with oxygen disorder at the 8*c* site, consistent with the phenomenon reported by Wang *et al.* [49]. The Raman spectrum of the REZO exhibits three characteristic peaks (E_g+2T_{2g}). Compared to GZO, the E_g peak intensity of the REZO is stronger, indicating an intermediate structural state between the ordered pyrochlore structure and the disordered fluorite structure.

Microstructure of the REZO ceramics was further examined by TEM. Figure 5a shows the high-angle annular dark-field (HAADF) images of the REZO and the EDS mapping of the corresponding elements. Evidently, all rare-earth elements are uniformly distributed in the REZO, indicating that the rare-earth atoms have completely dissolved into the crystal lattice of the pyrochlore and fluorite structures, contributing to the formation of a dual-phase HE-$RE_2Zr_2O_7$. Figure 5b shows the selected area electron diffraction (SAED) of the REZO, and the polycrystalline diffraction data demonstrate the coexistence of pyrochlore and fluorite structures, which is consistent with the XRD results. Figures 5c and 5e display the high-resolution transmission electron microscopy (HRTEM) images of fluorite and pyrochlore structures, respectively. It can be found that the lattice fringes with different orientations can be clearly observed, indicating that the REZO exhibits excellent crystallization behaviour. Figures 5g-5j show the corresponding magnified images of the g-j regions in Figs. 5c and 5e. The planar spacings in Figs. 5g and 5h are calculated to be 0.3025 and 0.2653 nm, respectively, which correspond well with the (111) and (200) planes of the fluorite structure. The interplanar spacings in Figs. 5i and 5j are calculated to be 0.3249 and 0.3058 nm, respectively, which match well with the (311) and (222) planes of the pyrochlore structure. Figure 5d presents the SAED patterns of the fluorite structure that correspond to the (002), $(1\bar{1}3)$, and $(1\bar{1}1)$ facets. Figure 5f shows the SAED patterns of the pyrochlore structure, corresponding to the $(1\bar{3}\bar{3})$, $(2\bar{4}0)$ and $(3\bar{5}3)$ facets.

Figure 6 shows the microtopography and corresponding elemental distributions of the sintered LZO, GZO and REZO. SEM images reveal that all samples exhibit relatively dense crystalline morphology with uniform grain distribution in the observed region. Table 4 lists the experimental and relative density of the different sintered samples. The experimental density measured by the Archimedes method for the LZO, GZO and REZO were 5.955, 6.632 and 6.723 g·cm^{-3}, respectively. The relative density of all samples exceeds 97%, indicating that the ceramic samples prepared by conventional solid-state reaction exhibit high sintered densities. In addition, the corresponding EDS mapping shows no obvious elemental segregation, indicating that the five rare-earth elements in the REZO sample are uniformly distributed within the pyrochlore and fluorite structures. Figure 7 shows the grain size of different samples. All samples have the grain size on the micrometer scale. Specifically, the average grain size of the REZO is 2.045 ± 0.772 µm, which is lower than that of the LZO (3.095 ± 0.653 µm) and GZO (3.657 ± 1.134 µm). The

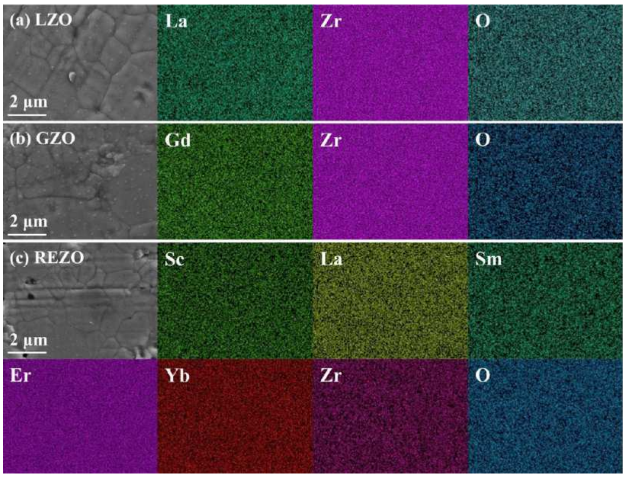

Figure 6. Microtopography and corresponding EDS mapping of: a) LZO, b) GZO and c) REZO

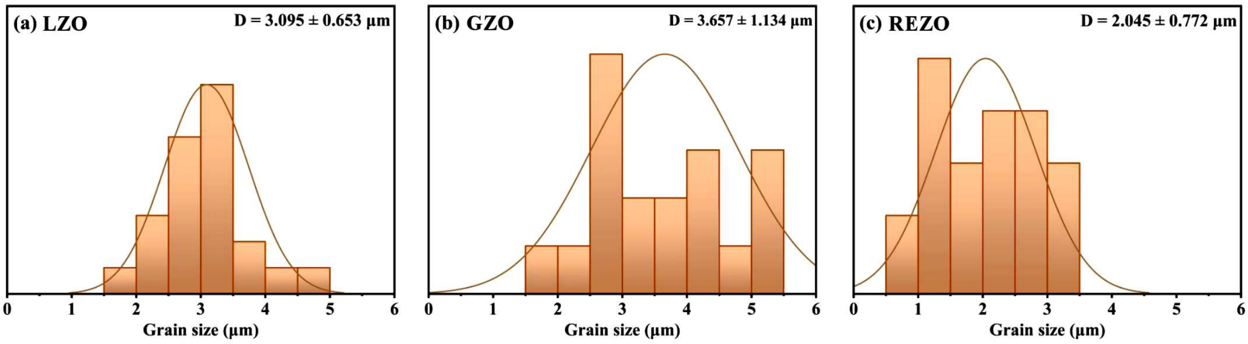

Figure 7. Grain size of: a) LZO, b) GZO and c) REZO

Table 4. The experimental density (ρ), relative density (ρ_r), and acoustic velocity (V_T, V_L and V_M) of LZO, GZO and REZO

Compounds	ρ [g/cm^3]	ρ_r [%]	V_T [m/s]	V_L [m/s]	V_M [m/s]
LZO	5.955	98.75	3720.29	6371.31	4125.76
GZO	6.632	98.25	3371.06	6026.16	3752.39
REZO	6.723	98.14	3094.51	5389.74	3436.59

grain refinement of the REZO sample was attributed to the sluggish diffusion effect. In addition, based on the report by Ren *et al.* [50], the coexistence of pyrochlore and fluorite structures can also inhibit the grain growth during the sintering process.

3.2. Thermophysical properties

Thermal conductivity is the most critical thermophysical property of thermal barrier coating materials. Lower thermal conductivity enables higher operating temperatures for hot-end components, significantly enhancing engine thrust-to-weight ratio and efficiency [51]. According to the Neumann-Kopp law, the specific heat capacity (C_p) of $RE_2Zr_2O_7$ can be calculated based on the component oxides and corresponding molar ratios, as shown below [52]:

$$C_p = \sum_{i=1}^{n} n_i C_{p,i} \tag{17}$$

$$C_{p,i} = A_1 + A_2 10^{-3} T + A_3 10^5 T^2 + A_4 10^{-6} T^3 + \\ + A_5 10^8 T^{-3} \tag{18}$$

where T represents temperature, n_i represents the molar fraction of the i-th element and $C_{p,i}$ represents the specific heat capacity of the i-th element as a function of T. The calculated values typically exhibit an error margin of less than 2% compared to actual measurements [53]. Figure 8a shows the specific heat capacity of three materials from room temperature to 1000 °C. It can be observed that in the low-temperature region, the specific heat capacity of all materials increases rapidly with the temperature rise, consistent with the relationship between the specific heat capacity and temperature in the Debye model [54]. As the temperature increases, the specific heat capacity of all samples continues to rise, approaching the limit value predicted by the Dulong-Petit law, which tends toward a temperature-independent constant [26].

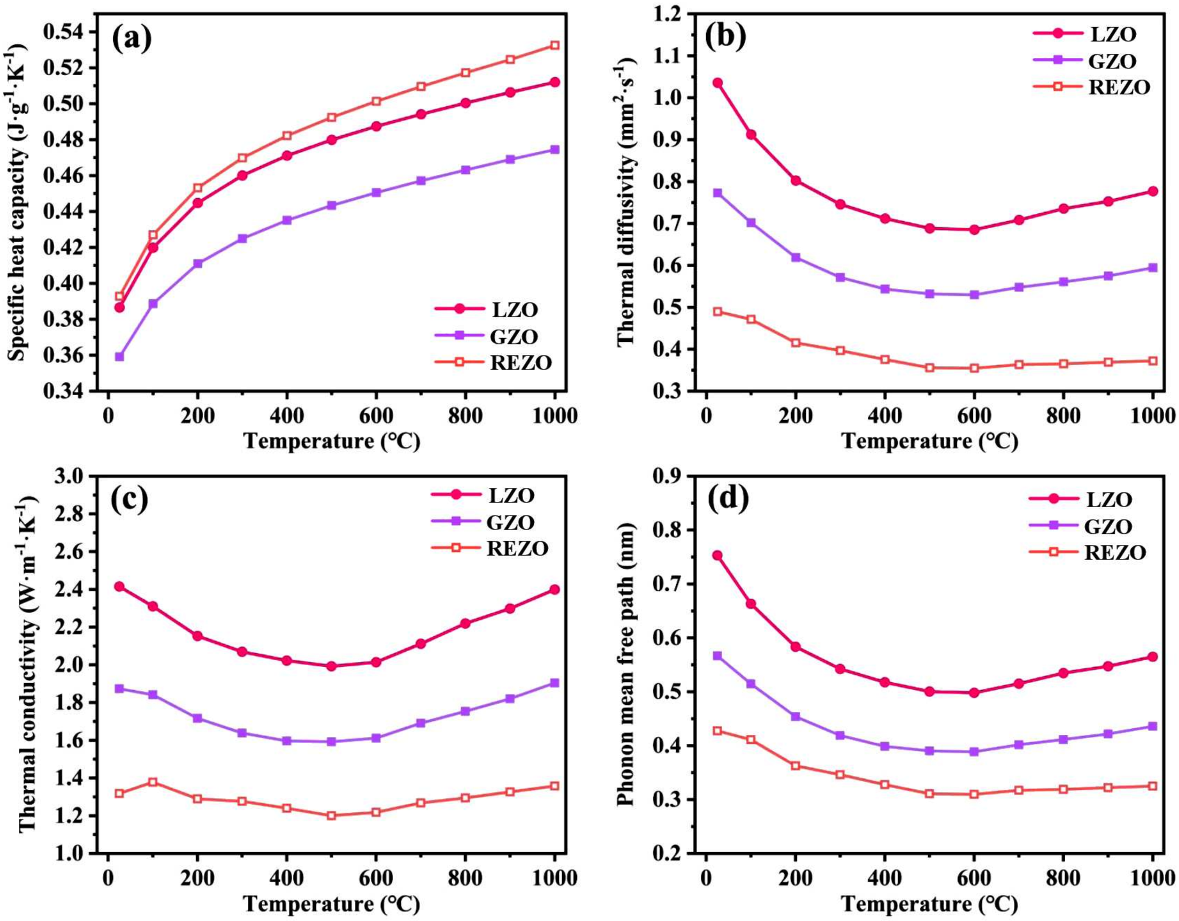

Figure 8. Thermal conductivity properties of LZO, GZO and REZO: a) specific heat capacity, b) thermal diffusivity, c) thermal conductivity and d) phonon mean free path

Figure 8b shows the thermal diffusivity (λ) of different samples from room temperature to 1000 °C. In the range from room temperature to 600 °C, the thermal diffusivity of all materials decreases with increasing temperature, consistent with the phonon heat transfer relationship $\lambda \propto (1/T)^n$ [55]. In the range of 600–1000 °C, the enhancement of radiation heat transfer leads to a significant increase in the thermal diffusivity of ceramic materials. Typically, the thermal diffusivity measured using the laser flash method contains both phonon heat transfer and radiation heat transfer. For infrared transmitting or semitransparent materials, heat transfer during the temperature rise process occurs not only through thermal conduction but also via infrared radiation directly passing through the material, and this part of heat transfer is referred to as radiation heat transfer [56]. Radiation heat transfer generally increases with rising temperature. The conventional YSZ materials exhibit significant radiation heat transfer only above 1500 °C [57]. However, due to the high infrared transmittance of $RE_2Zr_2O_7$, a significant radiation heat transfer phenomenon occurs already at approximately 600 °C [58]. Compared with $La_2Zr_2O_7$ and $Gd_2Zr_2O_7$, the REZO exhibits lower thermal diffusivity in the entire temperature range, which can be attributed to the effects of mass difference, size difference, and high-entropy effect. Additionally, the thermal diffusivity of the REZO exhibits minimal variation, indicating a different phonon scattering mechanism.

Figure 8c shows the thermal conductivity of LZO, GZO and REZO calculated at different temperatures based on Eqs. 11 and 12. The results show that the thermal conductivity of the REZO at room temperature is 1.31 $W \cdot m^{-1} \cdot K^{-1}$, less than half that of YSZ (3.06 $W \cdot m^{-1} \cdot K^{-1}$), and significantly lower than that of the LZO (2.41 $W \cdot m^{-1} \cdot K^{-1}$) and GZO (1.87 $W \cdot m^{-1} \cdot K^{-1}$). As temperature increases, the thermal conductivity of the REZO reaches its minimum value (1.20 $W \cdot m^{-1} \cdot K^{-1}$) at 500 °C. Subsequently, due to the enhanced thermal radiation, the thermal conductivity of the REZO sample increases slightly. It should be noted that the LZO and GZO samples exhibit typical ceramic polycrystalline thermal behaviour. In contrast, the thermal conductivity of the REZO resembles that of glass-like materials at high temperatures and remains stable with increasing temperature.

Based on the relationship between the phonon mean free path (l) and thermal diffusivity in the Debye model ($\lambda = V_m l/3$) [59], the phonon mean free path of three materials at different temperatures was calculated and shown in Fig. 8d. Since the mean acoustic velocity of ceramic materials remains stable across the entire temperature range, the phonon mean free path in the three ceramics exhibits a similar trend to that of the thermal diffusivity. At 600 °C, the minimum phonon mean free path of the REZO is 0.315, approaching the average interatomic distance ($\approx$ 0.3 nm) in the crystal structure of HE-$RE_2Zr_2O_7$ compounds, demonstrating the strongest phonon scattering. Additionally, due to the intensified thermal radiation in high-temperature environments, the phonon mean free path in $La_2Zr_2O_7$ and $Gd_2Zr_2O_7$ exhibits a significant rising trend, whereas the phonon mean free path of the REZO sample, shows minimal variation, demonstrating promising potential for application in thermal barrier coatings.

To further understand the thermal conductivity behaviour of the REZO ceramics, its intrinsic thermal conductivity was calculated using the Debye model. For insulating ceramic materials, the thermal conduction behaviour primarily consists of phonon heat transfer and thermal radiation. Among them, phonon is essentially a lattice wave with a specific frequency and wavelength that can propagate throughout the entire crystal. When multiple phonons with different frequencies superimpose, a wave packet with a narrow spatial range is formed. When the size of the wave packet is significantly smaller than the sample dimensions or the overall material size, it can be treated as a particle. Consequently, phonons exhibit both wave-like and particle-like properties and can propagate and scatter within the lattice [60]. In addition, phonons can also interact with each other, leading to the transfer and dissipation of momentum and energy. The phonon thermal conductivity (k_p) of insulating ceramic materials is similar to that of the gas, with the specific formula given as follows [59]:

$$k_p = \frac{1}{3} C_v V_m^2 \tau = \frac{1}{3} C_v V_m l \tag{19}$$

where C_v represents the specific heat capacity. When the temperature exceeds the Debye temperature, C_v approaches a temperature-independent constant. V_m represents the mean acoustic velocity, which is primarily influenced by atomic mass and interatomic interactions, and is independent of temperature. l and τ represent the phonon mean free path and phonon relaxation time, respectively. Therefore, for thermal barrier coating ceramic materials, reducing V_m and l is an effective approach to reduce thermal conductivity. At different temperatures, the phonon mean free path is influenced by multiple phonon scattering modes. Since all phonon scattering modes are independent and can be superimposed, the phonon mean free path can be expressed as [61]:

$$\frac{1}{l} = \frac{1}{l_{phonon}} + \frac{1}{l_{boundary}} + \frac{1}{l_{defect}} + \frac{1}{l_{other}} \tag{20}$$

where l_{phonon} represents phonon scattering caused by the lattice anharmonic vibrations, constituting an intrinsic scattering mechanism in ceramic materials, also recognized as Umklapp scattering. $l_{boundary}$ represents phonon scattering at grain boundaries. In this work, since the grain sizes of the three ceramics are much larger than the phonon mean free path, and phonon scattering at grain boundaries typically becomes significant only below 30 K, the effect of grain size on the phonon mean

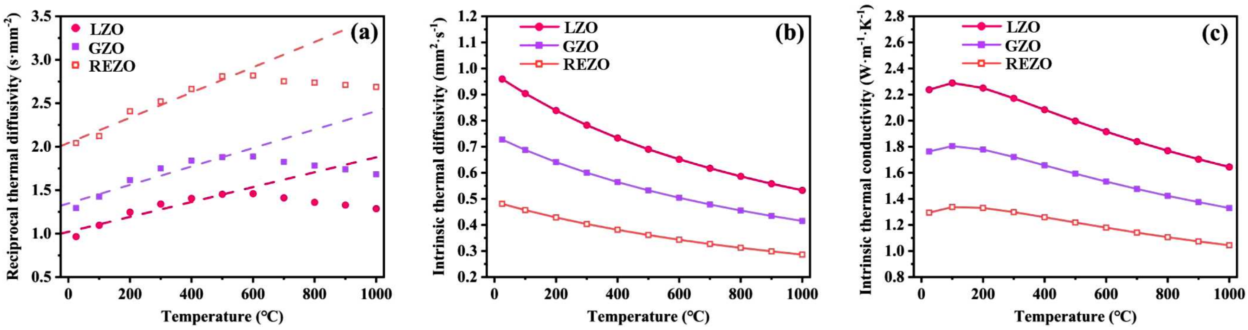

Figure 9. Reciprocal thermal diffusivity (a), intrinsic thermal diffusivity (b) and intrinsic thermal conductivity (c) of LZO, GZO and REZO

free path is neglected. l_{defect} represents phonon scattering at point defects, which usually dominates at low temperatures. l_{other} represents phonon scattering due to other mechanisms. In summary, Umklapp scattering is the primary factor influencing the phonon mean free path. Therefore, based on the relationship between the phonon mean free path and the thermal diffusivity in the Debye model, the phonon mean free path and thermal diffusivity at a given temperature (T) and frequency (ω) can be expressed as [62]:

$$\frac{1}{\lambda(\omega,T)} = \left(\frac{bCn^{\frac{1}{3}}}{\theta_D}\right)T + \left(D - \frac{1}{2}C\right) \tag{21}$$

where λ is the thermal diffusivity, θ_D is the Debye temperature, b is a constant approximately equal to 2, C and D are constants, and n is the number of atoms in the unit cell. Therefore, the reciprocal thermal diffusivity ($1/\lambda$) should theoretically be proportional to temperature. However, according to the test results in Fig. 8b, the thermal diffusivity of the three materials exhibits a clear linear relationship with $1/T$ only within the range of room temperature up to 600 °C. In the 600–1000 °C range, thermal diffusivity is affected by thermal radiation, causing a significant deviation from the linear relationship with $1/T$. To eliminate the influence of thermal radiation, linear fitting of $1/\alpha$ between room temperature to 600 °C was performed to determine the intrinsic thermal diffusivity of three ceramic materials. The fitting function is shown as the dashed line in Fig. 9a. Among them, the slope of the fitting function represents the degree of Umklapp scattering within the sample, with a higher slope indicating stronger phonon scattering. In this work, the slopes of the fitting functions for the three ceramic materials are ranked as follows: REZO (1.45×10^{-3}) > GZO (1.06×10^{-3}) > LZO (8.57×10^{-4}). Therefore, the REZO ceramics exhibits the lowest thermal diffusivity through the entire temperature range. Figures 9b and 9c show the intrinsic thermal diffusivity and intrinsic thermal conductivity calculated based on the fitted function, respectively. After eliminating the influence of thermal radiation, the thermal conductivity of REZO is only 1.04–1.33 $\text{W}\cdot\text{m}^{-1}\cdot\text{K}^{-1}$, lower than that of LZO and GZO. In summary, although the REZO ceramics exhibits increased thermal conductivity under high-temperature conditions, its low theoretical thermal conductivity and stable thermal conductivity behaviour make it suitable for application in thermal barrier coatings.

According to the relationship between thermal conductivity and temperature reported by Kim *et al.* [63], the degree of Umklapp scattering gradually increases with rising temperature, while phonon scattering in low-temperature environment is primarily influenced by point defects. The point defects include vacancy and substitutional atomic defects. The phonon mean free path can be regarded as the product of the acoustic velocity and the phonon relaxation time, while the relaxation time for phonon scattering with point defects (τ_P) can be expressed as [64,65]:

$$\begin{aligned} \frac{1}{\tau_P} &= \frac{V\omega^4}{4\pi v_p^2 v_g}\left(\sum if_i\left(1-\frac{M_i}{M}\right)^2\right) + \\ &+ \varepsilon \sum if_i\left(\sum if_i\left(1-\frac{R_i}{R}\right)^2\right) \end{aligned} \tag{22}$$

$$\varepsilon = \frac{2}{9}\left(6.4\gamma\frac{1+\nu}{1-\nu}\right)^2 \tag{23}$$

where V is the average atomic volume, ν is Poisson's ratio, γ is the anharmonic coefficient, f_i is the proportion of displaced atoms with mass M_i and radius R_i in a system with average atomic mass M and average atomic radius R, ω, v_p and v_g are the phonon angular frequency, phase velocity and group velocity, respectively. It can be observed that phonon scattering with point defects is independent of temperature. The greater the mass and radius difference between the doping atom and the matrix atom, the shorter the relaxation time of phonon scattering with point defects, and the shorter the phonon mean free path. In HE-$\text{RE}_2\text{Zr}_2\text{O}_7$, multiple atoms with varying masses and ionic radii occupy the same lattice site, leading to a significant lattice distortion. These mass and radius differences contribute to the strong point defect scattering. In this work, the $\Delta M/M$ ($\Delta R/R$) values for LZO, GZO and REZO are 0.956 (0.209), 1.006 (0.219) and 1.021 (0.227), respectively. Therefore, the REZO ceramics exhibits lower thermal conductivity under low-temperature conditions.

Oxygen vacancies as a characteristic point defect in

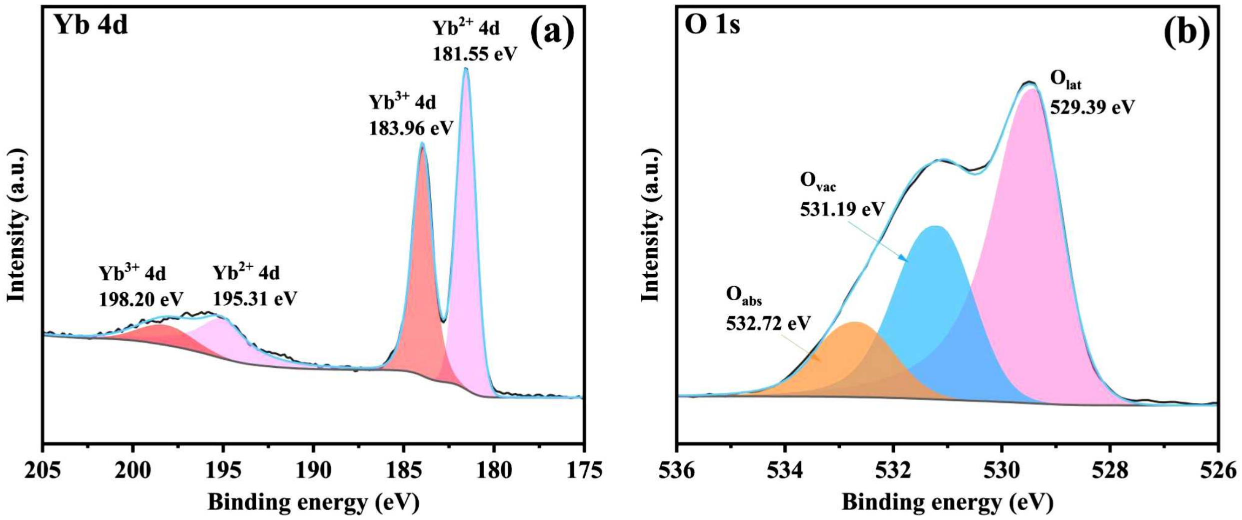

Figure 10. Yb 4*d* (a) and O 1*s* (b) XPS spectra of REZO

$RE_2Zr_2O_7$ also contribute to the phonon scattering at low temperatures. According to reports by Ma *et al.* [66], Yb^{3+} undergoes a transformation from the trivalent to the divalent state during high-temperature reactions, resulting in a significant increase in the amount of oxygen vacancies within the material. Therefore, XPS was employed to determine the valence states of the Yb element and the concentration of oxygen vacancies in the REZO sample. Figure 10a presents the XPS spectra of Yb 4*d* in REZO. The peaks at 183.96 and 198.20 eV correspond to Yb^{3+}, while the peaks at 181.55 and 195.31 eV originate from Yb^{2+}. It should be noted that due to a significant lattice distortion and structural disorder in the REZO sample, there is a redistribution of electron density around the anion. Consequently, the binding energies corresponding to the different oxidation states of Yb in this work exhibit slight deviations from those reported by Ma *et al.* [66]. Additionally, the valence state changes of Yb require the formation of additional intrinsic oxygen vacancies to maintain charge neutrality, as shown by Eq. 24:

$$2\,\mathrm{Yb}^{3+} \longrightarrow 2\,\mathrm{Yb}^{2+} + V_{\mathrm{O}}^{\bullet\bullet} \tag{24}$$

XPS spectrum of O 1*s* in the REZO sample is shown in Fig. 10b, where the peaks at 531.19, 532.72 and 529.39 eV correspond to oxygen vacancies, physically adsorbed oxygen, and lattice oxygen, respectively. Generally, the concentration of oxygen vacancies (O_{Vac}) in the REZO ceramics can be calculated using the peak area, with the specific calculation formula shown below:

$$Q_{vac} = \frac{A_{O_{vac}}}{A_{O_{vac}} + A_{O_{lat}} + A_{O_{abs}}} \tag{25}$$

where $A_{O_{abs}}$, $A_{O_{vac}}$ and $A_{O_{lat}}$ represent the peak area of physically adsorbed oxygen, oxygen vacancies and lattice oxygen, respectively. Based on the fitting results, the concentration of oxygen vacancies (O_{Vac}) of the REZO is 31.05%, which is higher than that of the LZO (12.5%) and GZO (12.5%) ceramics. Therefore, it can be concluded that the high concentration of oxygen vacancies in REZO enhances phonon scattering from point defects within the material, resulting in a lower thermal conductivity at low temperatures.

The linear expansion rate (dL/L_0) of three materials was tested from 100–1200 °C using a thermal dilatometer, and the results are shown in Fig. 11a. It can be observed that the LZO, GZO and REZO prepared in this work demonstrate excellent high-temperature phase stability. The linear expansion rate curve remains smooth throughout the entire temperature range tested and shows a strong linear relationship with temperature, without any noticeable peaks or abrupt changes. Figure 11b shows the thermal expansion coefficient (α) of different materials calculated based on Eq. 13. At low temperatures, the thermal expansion coefficient curve displays irregular fluctuations, which are attributed to the hysteresis effect in the thermal dilatometer. As the temperature increases, the thermal expansion coefficient curve gradually tends to smooth, indicating that the thermal expansion of the material gradually stabilizes. In addition, it can be observed that the thermal expansion coefficient of the REZO ($11.054 \times 10^{-6}\,K^{-1}$, 1200 °C) is higher than that of the LZO ($8.816 \times 10^{-6}\,K^{-1}$, 1200 °C) and GZO ($10.455 \times 10^{-6}\,K^{-1}$, 1200 °C).

Typically, thermal expansion in solid materials occurs during heating, and its thermal expansion behaviour is related to the asymmetry of lattice energy (U), as demonstrated by the lattice energy formula derived by Born-Landé [67]:

$$U = N_A \frac{Z^+ Z^-}{4\pi\varepsilon_0 r_0} A e^2 \left(1 - \frac{1}{n}\right) \tag{26}$$

where N_A, Z^+, Z^-, ε_0, r_0, A, e and n represent Avogadro's constant, cation charge, anion charge, vacuum permittivity, average cation-anion distance, Madelung constant, electronic charge and Born exponent. In this work, the average Shannon ionic radii of RE^{3+} sites in

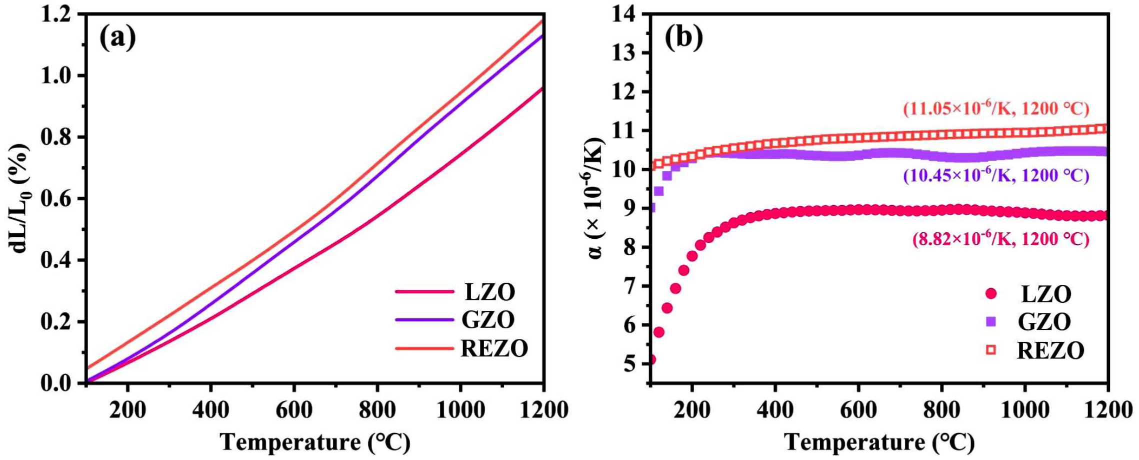

Figure 11. Thermal expansion properties of LZO, GZO and REZO: a) thermal expansion rate curves and b) thermal expansion coefficient curves

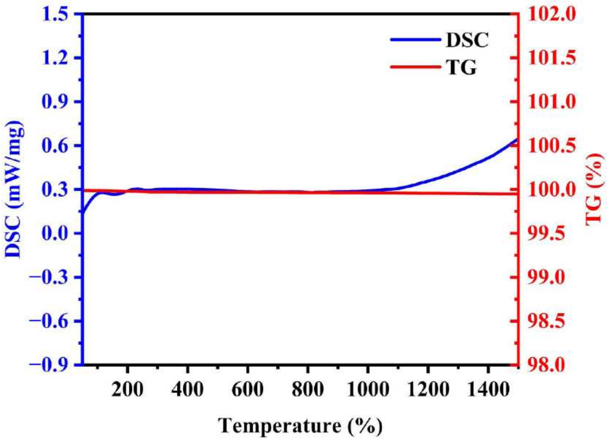

Figure 12. TG-DSC curves of REZO measured from room temperature to 1500 °C

three materials are ordered as: $r_{(REZO)} < r_{(GZO)} < r_{(LZO)}$. This lattice contraction leads to the increased lattice energy and reduced thermal expansion coefficient. However, according to the report of Luo *et al.* [68], the Madelung constant is also a crucial parameter affecting lattice energy, which decreases as the Madelung constant decreases. Kutty *et al.* [69] demonstrated that the Madelung constant for the pyrochlore structure decreases with increasing x-value of O_{48f}. According to the refinement results in Table 3, the x-values of O_{48f} in the pyrochlore structure for the REZO and $La_2Zr_2O_7$ samples are 0.3497 and 0.3541, respectively. Therefore, a higher x-value is one of the primary factors of reduced lattice energy, leading to the lattice relaxation and distortion of the $[ZrO_6]$ octahedra, resulting in a higher thermal expansion coefficient of the REZO ceramics.

Thermal barrier coatings exposed to high-temperature combustion gases may undergo phase transformation after prolonged exposure, which can affect the microstructure and stress state of the coatings. Therefore, the high-temperature phase stability is a crucial factor for assessing the durability of ceramic coatings. A preliminary assessment of the phase stability of REZO from room temperature to 1500 °C was conducted using TG-DSC. As shown in Fig. 12, the mass curve of REZO remains nearly linear below 1500 °C, with a mass change of only 0.17%. The DSC curve is similar to the TG curve, showing no significant endothermic or exothermic processes, indicating that REZO did not undergo phase transformation during heating. This result is consistent with that in Fig. 11a.

Since TG-DSC analysis is conducted within a limited period, it is primarily used to evaluate short-term phase stability. To characterize the long-term high-temperature phase stability of the REZO ceramics, it was calcined at 1600 °C for 50/100/150 h, respectively. The phase composition of REZO calcined for different times was examined, with results shown in Fig. 13a. The comparison analysis shows no additional diffraction peaks in the XRD patterns, even with the calcination time extended to 150 h, highlighting the outstanding phase stability of REZO under high-temperature conditions. Figure 13b shows the Raman spectrum of the REZO sample after calcination at 1600 °C for different times. No significant differences were observed in the Raman spectrum either, further confirming the outstanding high-temperature phase stability of the REZO sample.

3.3. Mechanical properties

Mechanical properties are one of the key performance parameters of TBCs, which significantly influence the high-temperature service life and reliability of the coating system [70]. Therefore, the Young's modulus (E), Vickers hardness (H_V) and fracture toughness (K_{IC}) of different materials were investigated. Table 4 lists the acoustic velocity (V_L, V_T and V_M) of LZO, GZO and REZO. The V_M of the REZO sample is 3436.59 m/s, lower than that of the LZO (4125.76 m/s) and GZO (3752.39 m/s), indicating that the interatomic bonding strength of the REZO is weaker than in LZO and GZO. Figure 14 shows the mechanical properties of different materials. The Young's modulus of the REZO ceramics is 161.48 ± 8.07 GPa, which is lower than that of the LZO (204.62 ± 10.23 GPa) and GZO

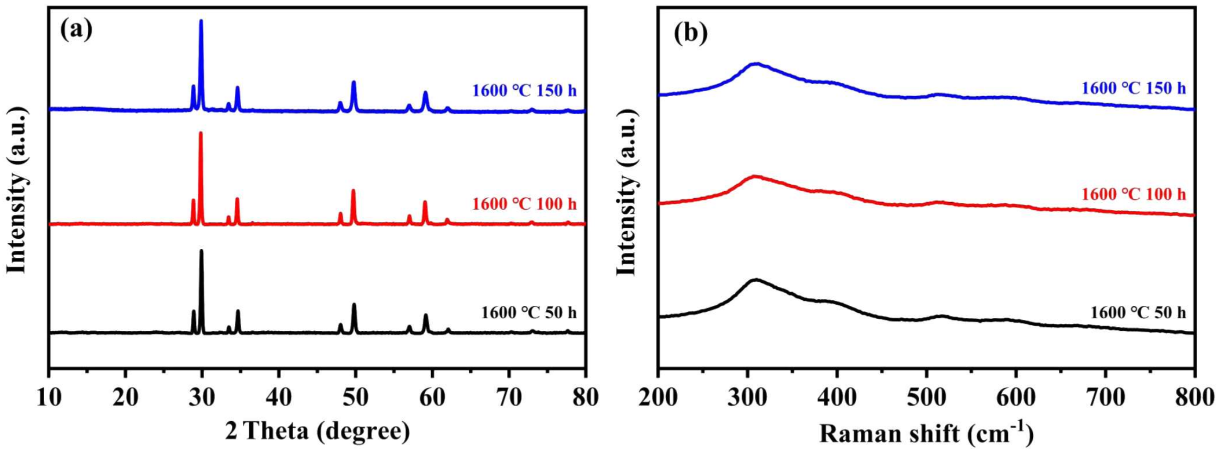

Figure 13. XRD patterns (a) and Raman spectra (b) of REZO after calcination at 1600 °C for different times

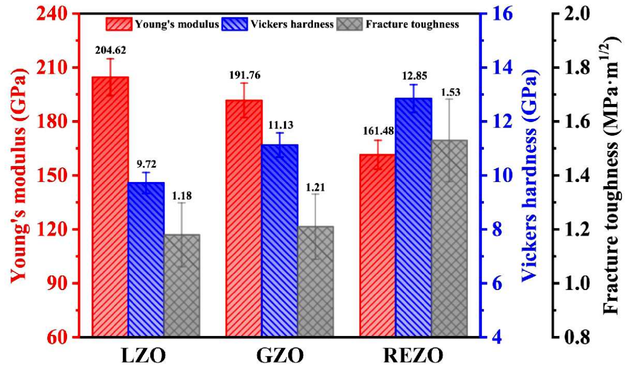

Figure 14. Young's modulus, Vickers hardness, and fracture toughness of LZO, GZO and REZO

(191.76 ± 9.59 GPa). The lower Young's modulus of REZO is attributed to various defects introduced by high-entropy design, including mass differences, ionic radius differences and oxygen vacancies. An increase in these defects leads to a relaxation of the lattice structure, which reduces the acoustic velocity and the Young's modulus [71]. For ceramic materials used in TBCs, a lower Young's modulus contributes to minimizing thermal stresses caused by mismatched thermal expansion coefficients during temperature fluctuations. This property enhances coating stability and extends its service life.

The Vickers hardness of the REZO sample is approximately 12.85 ± 0.54 GPa, which is higher than 9.72 ± 0.39 GPa for the LZO and comparable to 11.13 ± 0.45 GPa for the GZO ceramics. In terms of Vickers hardness, the hardness of oxide ceramics is a physical quantity influenced by multiple factors, including crystal structure, chemical composition and grain size. In terms of crystal structure, according to the reports by Plendl *et al.* [72], Vickers hardness is related to atomic distances and unit cell parameters. Since the RE–O bond length and unit cell parameters of the pyrochlore structure are larger than those of the fluorite structure, GZO exhibits a higher Vickers hardness than LZO. For REZO, since it is a dual-phase solid solution composed of 82.99% fluorite phase and 17.01% pyrochlore phase, it possesses a higher Vickers hardness than single-phase pyrochlore. In terms of chemical composition, the RE^{3+} sites in REZO consist of five rare-earth cations with different sizes, including a Shannon ionic radius difference of 29 pm between Sc^{3+} and La^{3+}. This size difference caused by different rare-earth cations leads to significant distortion in the anion sublattice. Figure 15 displays the HRTEM and corresponding Fourier transform (FFT) images of the REZO ceramics at different locations. It can be observed that the lattice fringes in REZO display a clearly visible lattice distortion. This distortion enhances resistance to dislocation motion, restricts slip and plastic deformation, thereby increasing the Vickers hardness of the ceramic material. Additionally, according to reports by Sarker *et al.* [73], significant mass differences in high-entropy ceramics cause the energy required for dislocation motion to scatter and disrupt. This energy scattering mechanism increases the mechanical work needed for plastic deformation in high-entropy ceramics, resulting in enhanced hardness of the ceramic solid solution. In this work, the mass difference in REZO reaches 1.021, exceeding that in LZO (1.006) and GZO (0.956). Consequently, the stronger energy scattering in the REZO sample contributes to the enhancement of its Vickers hardness. The grain size of ceramic materials is also a key factor influencing hardness. According to the report by Maita *et al.* [74], grain boundaries in ceramic materials endure greater stress during external impacts. As a result, a higher density of grain boundaries is associated with increased hardness in ceramic materials. Generally, smaller ceramic grain sizes lead to a higher density of grain boundaries. In this work, the grain size of the REZO sample is 2.045 ± 0.772 µm, smaller than that of the LZO (3.095 ± 0.653 µm) and GZO (3.657 ± 1.134 µm) ceramics, resulting in higher grain boundary density and consequently higher Vickers hardness for the REZO sample.

Fracture toughness is an essential parameter in materials mechanics, as it characterizes a material's ability to resist the propagation of cracks. In this work, the fracture toughness of REZO is 1.53±0.15 MPa·m$^{1/2}$, ex-

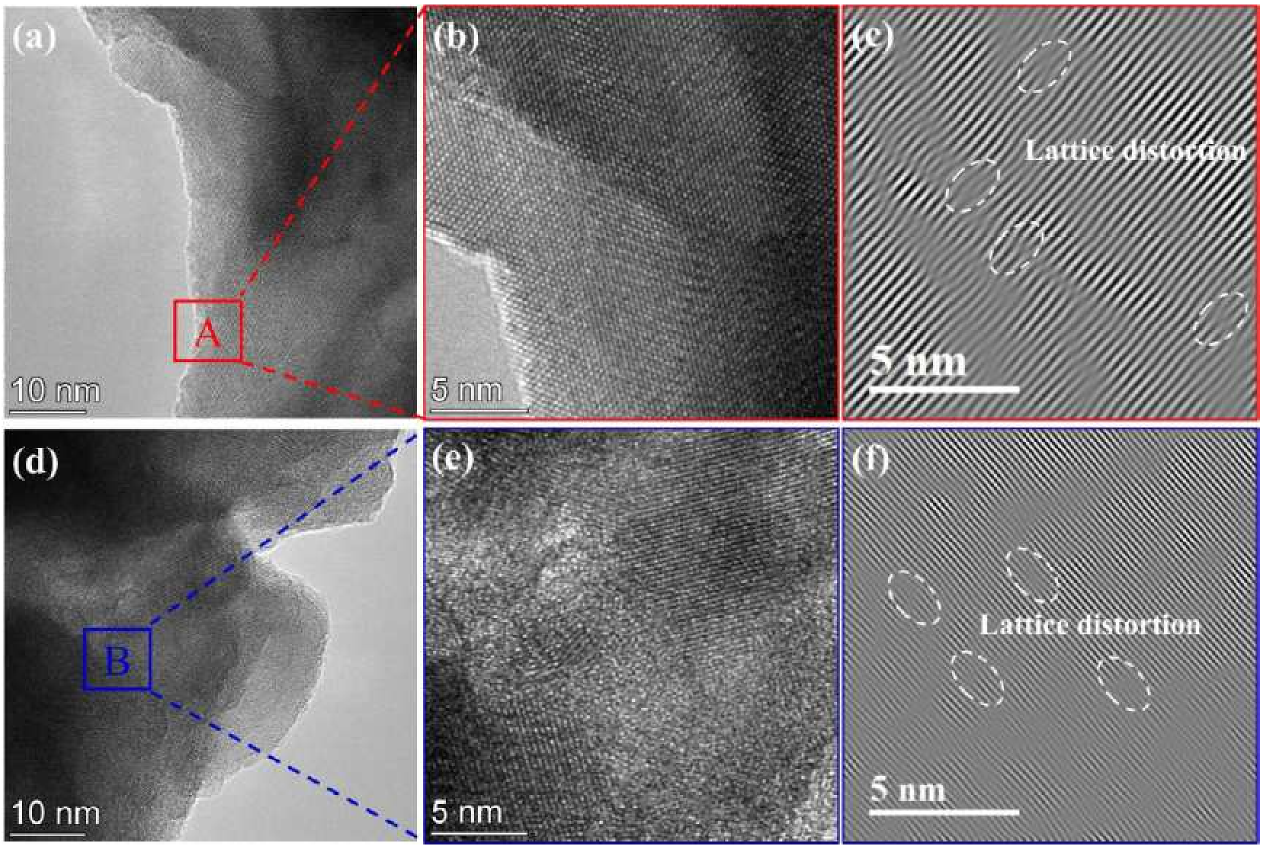

Figure 15. HRTEM images of REZO (a,d), HRTEM image and corresponding Fourier transform image of region A (b,e) and HRTEM image and corresponding Fourier transform image of region B (c,f)

ceeding that of LZO (1.18 ± 0.12 MPa·m$^{1/2}$) and comparable to that of GZO (1.21 ± 0.12 MPa·m$^{1/2}$). According to the report by Zhang *et al.* [75], the fracture toughness of ceramic materials is related to the fracture energy and cohesion energy. Since the REZO sample exhibits a dual-phase structure, it exhibits a significant degree of lattice distortion within its structure. Consequently, the REZO ceramics demonstrates high cohesion energy and fracture energy, resulting in a higher fracture toughness.

IV. Conclusions

This work is based on the thermal properties tailoring theory in high-entropy rare-earth zirconates (HE-$RE_2Zr_2O_7$). By leveraging the phonon scattering mechanism and the correlation between thermal expansion behaviour and electronegativity, a novel high-entropy $(Sc_{0.2}La_{0.2}Sm_{0.2}Er_{0.2}Yb_{0.2})_2Zr_2O_7$ (REZO) ceramics was designed and prepared by conventional solid-state reaction. The phase composition, microstructure, thermophysical properties, and mechanical properties were systematically investigated and compared with those of the single-component $La_2Zr_2O_7$ (LZO) and $Gd_2Zr_2O_7$ (GZO) ceramics. The main conclusions of the work are as follows:

1. Based on phonon scattering theory and thermal expansion theory, a novel composition design method for HE-$RE_2Zr_2O_7$ is proposed. By controlling mass differences, size differences, and electronegativity, customized composition design and performance optimization of HE-$RE_2Zr_2O_7$ are achieved.
2. REZO crystal structure contains 82.99% fluorite phase and 17.01% pyrochlore phase because of higher size disorder in REZO. SEM and TEM confirm that all rare-earth elements are uniformly distributed in REZO without compositional segregation. Also, under the combined effects of sluggish diffusion and the dual-phase structure, the average grain size of REZO is 2.045 ± 0.772 µm, smaller than that of LZO (3.095 ± 0.653 µm) and GZO (3.657 ± 1.134 µm).
3. Compared to LZO and GZO, REZO exhibits superior thermal insulation properties and thermal expansion behaviour. The significant mass difference, size difference, and additional oxygen vacancies within REZO increase the phonon scattering, resulting in optimized low-temperature thermal insulation performance. Meanwhile, the enhanced Umklapp scattering in REZO contributes to the reduced thermal conductivity at high temperatures, resulting in glass-like thermal conductivity in the entire temperature range. Also, the thermal expansion coefficient (TEC) of REZO at 1200 °C is $11.054\times10^{-6}\,K^{-1}$, higher than that of LZO ($8.816\times10^{-6}\,K^{-1}$) and GZO ($10.455\times10^{-6}\,K^{-1}$). This is attributed to the higher x-value (0.3562) of the O_{48f} site in the pyrochlore phase, which reduces lattice energy and induces distortion of the $[ZrO_6]$ octahedra. High-temperature stability

tests demonstrate that REZO exhibits excellent phase stability from room temperature to 1600 °C.

In terms of mechanical properties, the Young's modulus of the REZO sample was 161.48 ± 8.07 GPa, lower than that of the LZO (204.62 ± 10.23 GPa) and GZO (191.76 ± 9.59 GPa) ceramics. Additionally, under the combined effects of the dual-phase structure strengthening, the mass and size differences of rare-earth cations, and grain refinement strengthening, the Vickers hardness of REZO reached 12.85 ± 0.54 GPa, higher than that of LZO (9.72 ± 0.39 GPa) and approaching to that of GZO (11.13 ± 0.45 GPa). Also, the fracture toughness of REZO reached 1.53 ± 0.15 MPa·m$^{1/2}$, outperforming LZO (1.18 ± 0.12 MPa·m$^{1/2}$) and GZO (1.21 ± 0.12 MPa·m$^{1/2}$). This result is closely related to the high cohesion energy and fracture energy conferred by the dual-phase structure.

Acknowledgement: The authors are thankful for the support of the National Natural Science Foundation of China (No. 51702145), the National Natural Science Foundation of China (No. 52371066), the University of Science and Technology Liaoning Graduate Student Innovation and Technology Project (LKDYC202501), and the Fundamental Research Funds for the Liaoning Universities fund (LJ212410146043).

References

1. T. Samarasinghe, C. Abeykoon, A. Turan, "Modelling of heat transfer and fluid flow in the hot section of gas turbines used in power generation: A comprehensive survey", *Int. J. Energy Res.*, **43** [5] (2019) 1647–1669.
2. G.E. Marin, B.M. Osipov, A.V. Titov, A.R. Akhmetshin, "Simulation of the operation of a gas turbine installation of a thermal power plant with a hydrogen fuel production system", *Int. J. Hydrogen Energy*, **48** [12] (2023) 4543–4550.
3. L. Heber, J. Schwab, "Modelling of a thermoelectric generator for heavy-duty natural gas vehicles: Techno-economic approach and experimental investigation", *Appl. Therm. Eng.*, **174** (2020) 115156.
4. A.E. Alali, Z.B. Abulawi, A.M. Obeidat, "Assessment of thermal performance improvement of GT-MHR by waste heat utilization in power generation and hydrogen production", *Int. J. Hydrogen Energy*, **46** [44] (2021) 22719–2734.
5. M. Galati, M. Giordano, A. Saboori, S. Defanti, "Electron beam powder bed fusion of Ti-6Al-2Sn-4Zr-2Mo lattice structures: morphometrical and mechanical characterisations", *Int. J. Adv. Des. Manuf. Technol.*, **131** [3] (2024) 1223–1239.
6. J.Y. Jeong, Y.R. Jo, M.S. Kang, Y.J. Kang, J.S. Kwak, "Film cooling effectiveness and flow structures of butterfly-shaped film cooling hole configuration", *J. Therm. Sci. Eng. Appl.*, **16** [3] (2024) 031009.
7. J.H. Liu, Z. Lu, Y.W. Zhou, J. Zhang, G.L. Lyu, "A review on the failure behavior and countermeasures of thermal barrier coatings", *J. Ceram. Process. Res.*, **24** [2] (2023) 285–307.
8. B. Gleeson, "Thermal barrier coatings for aeroengine applications", *J. Propul. Power*, **22** [2] (2006) 375–383.
9. X.Q. Cao, R. Vassen, D. Stoever, "Ceramic materials for thermal barrier coatings", *J. Eur. Ceram. Soc.*, **24** [1] (2004) 1–10.
10. J. Wang, L.Y. Bai, F. Ma, S.H. Wan, G.W. Yi, J. Sun, X.W. Tian, Z.H. Yang, "Evaluation of microstructure evolution of thermal barrier YSZ coating after thermal exposure", *Ceram. Int.*, **48** [5] (2022) 6681–6690.
11. Z.J. Peng, Y.H. Wang, S.Q. Wang, J.T. Yao, Q.Y. Zhao, E.Y. Xie, G.L. Chen, Z.G. Wang, Z.G. Liu, Y.M. Wang, J.H. Ouyang, "Improvement strategy on thermophysical properties of $A_2B_2O_7$-type rare earth zirconates for thermal barrier coatings applications: A review", *Int. J. Miner. Metall. Mater.*, **31** [5] (2024) 1147–1165.
12. Y.J. Wang, L. Zhang, W.J. Wu, J. Yang, "Enhancement of thermal properties of ytterbium-cerium oxide by zirconium doping for thermal barrier coatings", *Philos. Mag. Lett.*, **99** [9] (2019) 309–316.
13. J. Feng, B. Xiao, R. Zhou, W. Pan, "Thermal expansion and conductivity of $RE_2Sn_2O_7$ (RE = La, Nd, Sm, Gd, Er and Yb) pyrochlores", *Scr. Mater.*, **69** [5] (2013) 401–404.
14. L. Chen, M.Y. Hu, J. Guo, X.Y. Chong, J. Feng, "Mechanical and thermal properties of $RETaO_4$ (RE = Yb, Lu, Sc) ceramics with monoclinic-prime phase", *J. Mater. Sci. Technol.*, **52** (2020) 20–28.
15. C.L. Wan, W. Zhang, Y.F. Wang, Z.X. Qu, A.B. Du, R.F. Wu, W. Pan, "Glass-like thermal conductivity in ytterbium-doped lanthanum zirconate pyrochlore", *Acta Mater.*, **58** [18] (2010) 6166–6172.
16. X.Y. Guo, Z. Lu, H.Y. Park, L. Li, J. Knapp, Y.G. Jung, J. Zhang, "Thermal properties of $La_2Zr_2O_7$ double-layer thermal barrier coatings", *Adv. Appl. Ceram.*, **118** [3] (2019) 91–97.
17. Z.H. Xu, L.M. He, R.D. Mu, X. Zhou, "$(Y_{0.05}La_{0.95})_2(Zr_{0.7}Ce_{0.3})_2O_7$ ceramics as a thermal barrier coating material for high-temperature applications", *Mater. Lett.*, **116** (2014) 182–184.
18. Y.F. Wang, F. Yang, P. Xiao, "Role and determining factor of substitutional defects on thermal conductivity: A study of $La_2(Zr_{1-x}B_x)_2O_7$ (B = Hf, Ce, $0 \leq x \leq 0.5$) pyrochlore solid solutions", *Acta Mater.*, **68** (2014) 106–115.
19. J.W. Yeh, S.K. Chen, S.J. Lin, J.Y. Gan, T.S. Chin, T.T. Shun, C.H. Tsau, S.Y. Chang, "Nanostructured high-entropy alloys with multiple principal elements: Novel alloy design concepts and outcomes", *Adv. Eng. Mater.*, **6** [5] (2004) 299–303.
20. B. Cantor, I.T.H. Chang, P. Knight, A.J.B. Vincent, "Microstructural development in equiatomic multicomponent alloys", *Mater. Sci. Eng. A*, **375** (2004) 213–218.
21. C.M. Rost, E. Sachet, T. Borman, A. Moballegh, E.C. Dickey, D. Hou, J.L. Jones, S. Curtarolo, J.P. Maria, "Entropy-stabilized oxides", *Nat. Commun.*, **6** (2015) 5485.
22. Y.W. Ding, K.J. Ren, C. Chen, L. Huan, R.L. Gao, X.L. Deng, G. Chen, W. Cai, C.L. Fu, Z.H. Wang, X. Lei, "High-entropy perovskite ceramics: Advances in structure and properties", *Process. Appl. Ceram.*, **18** [1] (2024) 1–11.
23. Q. Yin, K.H. Shen, Y. Wang, Y.Z. Xing, "Research progress of rare earth zirconate thermal barrier coating ceramic materials", *Mater. Today Commun.*, **42** (2025) 111579.
24. J.H. Liu, Y.Y. Wang, Z. Lu, Y.W. Zhou, Y. Li, J. Zhang,

G. Lyu, Y.G. Jung, "A review of the high-entropy ceramic materials for thermal barrier coatings: Design, synthesis, sintering and properties", *Process. Appl. Ceram.*, **19** [1] (2025) 1–25.

25. X.W. Luo, S. Huang, R.Q. Huang, C.H. Xu, S. Hou, H.Y. Jin, "Highly anti-sintering and toughened pyrochlore $(Dy_{0.2}Nd_{0.2}Sm_{0.2}Eu_{0.2}Yb_{0.2})_2Zr_2O_7$ high-entropy ceramic for advanced thermal barrier coatings", *Ceram. Int.*, **49** [14] (2023) 23410–23416.
26. Z.F. Zhao, Z.Y. Ruan, R. Li, Y.S. Yan, X.L. Sun, C. Liu, D. Zhang, B. Xu, Z.Y. Ren, M. Wang, J.Y. Li, J. Tian, Y.H. Jiang, J. Feng, Y.C. Zhou, "High entropy pyrochlore $(La_{0.3}Gd_{0.3}Ca_{0.4})_2(Ti_{0.2}Zr_{0.2}Hf_{0.2}Nb_{0.2}Ta_{0.2})_2O_7$ ceramic with amorphous-like thermal conductivity for environmental/thermal barrier coating applications", *J. Mater. Sci. Technol.*, **205** (2025) 315–326.
27. W.K. Fan, X. Yang, H.H. Li, Y. Li, J.T. Li, "Pressureless sintering of $(Y_{0.2}Gd_{0.2}Er_{0.2}Yb_{0.2}Lu_{0.2})_2Zr_2O_7$ high-entropy ceramic and Its high temperature CMAS corrosion resistance", *J. Inorg. Mater.*, **40** [2] (2025) 159–167.
28. J.G. Thakare, C. Pandey, M.M. Mahapatra, R.S. Mulik, "Thermal barrier coatings - A state of the art review", *Met. Mater. Int.*, **27** [7] (2021) 1947–1968.
29. L.R. Luo, W. Wang, L. Wang, F.W. Guo, Y.B. Sun, P.P. Wang, H. Zhang, J. Lu, X.F. Zhao, "Understanding of the composition-structure-properties relationships in high-entropy rare earth zirconates", *J. Eur. Ceram. Soc.*, **45** [5] (2025) 117103.
30. A. Rauf, Q. Yu, L. Jin, C. Zhou, "Microstructure and thermal properties of nanostructured lanthana-doped yttria-stabilized zirconia thermal barrier coatings by air plasma spraying", *Scr. Mater.*, **66** [2] (2012) 109–112.
31. O. Maulik, D. Kumar, S. Kumar, S.K. Dewangan, V. Kumar, "Structure and properties of lightweight high entropy alloys: a brief review", *Mater. Res. Express*, **5** [5] (2018) 052001.
32. J.H. Liu, Y. Li, Z. Lu, J.S. Lee, Y.G. Jung, H. Choi, Y.W. Zhou, H. Chen, "Reactive spark plasma sintering of a dual-phase high-entropy $(La_{0.2}Gd_{0.2}Sm_{0.2}Er_{0.2}Yb_{0.2})_2Zr_2O_7$ ceramic for thermal barrier coatings", *J. Korean Ceram. Soc.*, **62** [5] (2025) 934–949.
33. F.X. Ye, Y. Yao, F.W. Meng, Z.Q. Song, "A new B-site doped mid-entropy ceramic $Gd_2(Ti_{1/3}Zr_{1/3}Sn_{1/3})_2O_7$ for high-temperature thermal barrier coatings applications: Preparation process, thermophysical properties, and mechanical properties", *J. Alloys Compd.*, **1038** (2025) 182667.
34. X.W. Luo, R.Q. Huang, C.H. Xu, S. Huang, S. Hou, H.Y. Jin, "Designing high-entropy rare-earth zirconates with tunable thermophysical properties for thermal barrier coatings", *J. Alloys Compd.*, **926** (2022) 166714.
35. J.Y. Cao, M. Zhang, X.Y. Ma, S.T. Zhao, T. Jiang, W. Wen, "Synthesis and thermal behavior of rare-earth-niobate ceramics with fluorite structure", *Ceram. Int.*, **50** [21] (2024) 42299–42308.
36. K.Y. Li, S. Huang, S. Zhang, H.Y. Jin, "A novel sintering resistant $Sr(Eu_{0.2}Ho_{0.2}Er_{0.2}Tm_{0.2}Yb_{0.2})_2O_4$ high-entropy ceramic with superior thermophysical properties for advanced thermal barrier coatings", *J. Eur. Ceram. Soc.*, **45** [2] (2025) 116909.
37. J.K. Wang, L. Chen, G. Wang, S.X. Zhao, B. Yuan, H.X. Li, X.L. Chen, B.H. Li, L.Y. Zhang, J. Feng, "Dual-phase zirconate/tantalate high-entropy ceramics boost thermal properties and fracture toughness for thermal barrier coating materials", *J. Mater. Res. Technol.*, **32** (2024) 3825–3830.
38. J. Leitner, P. Vonka, D. Sedmidubsky, P. Svoboda, "Application of Neumann-Kopp rule for the estimation of heat capacity of mixed oxides", *Thermochim. Acta*, **497** [1] (2010) 7–13.
39. H. Zhan, W. Ma, X.X. Han, W.C. Liang, J.J. Hao, H.Y. Dong, Y. Bai, H.X. Liu, X.F. Meng, "A new type of $Sr(Zr_{0.2}Hf_{0.2}Ce_{0.2}Yb_{0.2}Me_{0.2})O_{3-x}$ (Me = Y, Gd) high-entropy ceramics used in thermal barrier coatings", *Int. J. Appl. Ceram. Technol.*, **20** [3] (2023) 1764–1773.
40. H.L. Liu, S. Pang, C.Q. Liu, Y.T. Wu, G.J. Zhang, "High-entropy yttrium pyrochlore ceramics with glass-like thermal conductivity for thermal barrier coating application", *J. Am. Ceram. Soc.*, **105** [10] (2022) 6437–6448.
41. W.W. Shuai, W. Qian, Z.C. Guan, Z.B. Li, Y.Q. Hua, J. Cai, "A novel dual-phase high-entropy $(La_{0.2}Nd_{0.2}Gd_{0.2}Er_{0.2}Yb_{0.2})_2Zr_2O_7$ ceramic for thermal barrier coatings applications: Preparation, microstructure, and thermos-physical properties", *Ceram. Int.*, **50** [7] (2024) 10525–10534.
42. Z. Teng, Y.Q. Tan, S.F. Zeng, Y. Meng, C. Chen, X.C. Han, H.B. Zhang, "Preparation and phase evolution of high-entropy oxides $A_2B_2O_7$ with multiple elements at A and B sites", *J. Eur. Ceram. Soc.*, **41** [6] (2021) 3614–3620.
43. T.T. Huang, Y.F. Liu, W. Fan, X.B. Zhong, R. Zou, F. Li, T. Song, T.X. Su, Y. Bai, "Investigations on the mechanical and thermal properties of multicomponent dual-phase rare-earth zirconate ceramics", *J. Alloys Compd.*, **1007** (2024) 176425.
44. W. Fan, Y. Bai, Y.F. Liu, T.T. Li, B.M. Li, L. Zhang, C.M. Gao, S.Y. Shan, H.C. Han, "Principal element design of pyrochlore-fluorite dual-phase medium- and high-entropy ceramics", *J. Mater. Sci. Technol.*, **107** (2022) 149–154.
45. Z. Chen, X.F. Cui, Y.Z. Jing, G. Jin, X. Wang, Y.C. Fang, X.H. Wang, D.C. Liu, B. Wang, "High temperature performance of $RE_2Zr_2O_7$ high-entropy ceramics designed by thermophysical performance-oriented principle", *Ceram. Int.*, **50** [9] (2024) 16499–16510.
46. M. de los Reyes, K.R. Whittle, Z.M. Zhang, S.E. Ashbrook, M.R. Mitchell, L.Y. Jang, G.R. Lumpkin, "The pyrochlore to defect fluorite phase transition in $Y_2Sn_{2-x}Zr_xO_7$", *RSC Adv.*, **3** [15] (2013) 5090–5099.
47. M. Glerup, O.F. Nielsen, F.W. Poulsen, "The structural transformation from the pyrochlore structure, $A_2B_2O_7$, to the fluorite structure, AO_2, studied by Raman spectroscopy and defect chemistry modeling", *J. Solid State Chem.*, **160** [1] (2001) 25–32.
48. M. Jafar, S.B. Phapale, B.P. Mandal, M. Roy, S.N. Achary, R. Mishra, A.K. Tyagi, "Effect of temperature on phase evolution in $Gd_2Zr_2O_7$: A potential matrix for nuclear waste immobilization", *J. Alloys Compd.*, **867** (2021) 159032.
49. Y.G. Wang, B. Gao, Q. Wang, X.H. Li, Z. Su, A.M. Chang, "$A_2Zr_2O_7$ (A = Nd, Sm, Gd, Yb) zirconate ceramics with pyrochlore-type structure for high-temperature negative temperature coefficient thermistor", *J. Mater. Sci.*, **55** [32] (2020) 15405–15414.
50. X.R. Ren, C.L. Wan, M. Zhao, J. Yang, W. Pan, "Mechanical and thermal properties of fine-grained quasi-eutectoid $(La_{1-x}Yb_x)_2Zr_2O_7$ ceramics", *J. Eur. Ceram. Soc.*, **35** [11] (2015) 3145–3154.

51. F.A. Guo, N. Trannoy, D. Gerday, “An application of scanning thermal microscopy: Analysis of the thermal properties of plasma-sprayed yttria-stabilized zirconia thermal barrier coating”, *J. Eur. Ceram. Soc.*, **25** [7] (2005) 1159–1166.
52. L.J. Tian, F. Peng, X.M. Song, W. Zheng, Z.W. Liu, Y.L. Huang, Y. Zeng, “Enhancing the thermodynamic properties of rare-earth niobates through high-entropy and composite engineering”, *Ceram. Int.*, **50** [11] (2024) 19488–19501.
53. Z.G. Liu, J.H. Ouyang, Y. Zhou, “Heat capacity measurements on $Yb_xGd_{2-x}Zr_2O_7$ (x = 0, 1, 2) ceramics by differential scanning calorimetry”, *Bull. Mater. Sci.*, **32** [6] (2009) 603–606.
54. D. Abdullah, D.C. Gupta, “DFT simulations of the elastic, optoelectronic, and thermoelectric attributes of $AOsCl_3$ (A = K, Rb), a robust and environmentally friendly perovskites for green energy implications”, *Sci. Rep.*, **14** [1] (2024) 26168.
55. L.P. Lai, M.D. Gan, J. Wang, L. Chen, X.B. Liang, J. Feng, X.Y. Chong, “New class of high-entropy rare-earth niobates with high thermal expansion and oxygen insulation”, *J. Am. Ceram. Soc.*, **106** [7] (2023) 4343–4357.
56. J.J. He, G. He, P.P. Wang, L.R. Xu, J. Liu, J.C. Tao, “Pyrochlore-fluorite dual-phase high-entropy $RE_2(Ce_{0.2}Zr_{0.2}Hf_{0.2}Sn_{0.2}Ti_{0.2})_2O_7$ ($RE_2HE_2O_7$, RE = La, Nd, Sm, Eu, Gd, Dy) ceramics with glass-like thermal conductivity”, *J. Mater. Sci.*, **57** [37] (2022) 17563–17576.
57. N.P. Padture, M. Gell, E.H. Jordan, “Thermal barrier coatings for gas-turbine engine applications”, *Science*, **296** [5566] (2002) 280–284.
58. M. Zhao, W. Pan, C.L. Wan, Z.X. Qu, Z. Li, J. Yang, “Defect engineering in development of low thermal conductivity materials: A review”, *J. Eur. Ceram. Soc.*, **37** [1] (2017) 1–13.
59. Y.L. Huang, Z.Y. Chen, Y.F. Xiong, J.J. Wu, C.C. Lin, W. Zheng, C.F. Jiang, Y. Zeng, “Investigation of thermal properties of rare-earth X2-Type monosilicates through high-entropy design and defect engineering”, *Ceram. Int.*, **51** [2] (2025) 1479–1789.
60. P.G. Klemens, M. Gell, “Thermal conductivity of thermal barrier coatings”, *Mater. Sci. Eng., A*, **245** [2] (1998) 143–149.
61. D. Song, T. Song, U. Paik, G. Lyu, Y.G. Jung, H.B. Jeon, Y.S. Oh, “Glass-like thermal conductivity in mass-disordered high-entropy $(Y,Yb)_2(Ti,Zr,Hf)_2O_7$ for thermal barrier material”, *Mater. Des.*, **210** (2021) 110059.
62. F.S. Wu, P. Wu, R.F. Zong, J. Feng, “Investigation on thermo-physical and mechanical properties of $Dy_3(Ta_{1-x}Nb_x)O_7$ ceramics with order-disorder transition”, *Ceram. Int.*, **45** [12] (2019) 15709–15710.
63. W. Kim, “Strategies for engineering phonon transport in thermoelectrics”, *J. Mater. Chem. C*, **3** [40] (2015) 10336–10348.
64. C.L. Wan, W. Pan, Q. Xu, Y.X. Qin, J.D. Wang, Z.X. Qu, M.H. Fang, “Effect of point defects on the thermal transport properties of $(La_xGd_{1-x})_2Zr_2O_7$: Experiment and theoretical model”, *Phys. Rev. B*, **74** [14] (2006) 144109.
65. J.D. Chung, A.J.H. McGaughey, M. Kaviany, “Role of phonon dispersion in lattice thermal conductivity modeling”, *J. Heat Transfer*, **126** [3] (2004) 376–380.
66. Y. Ma, X.B. Zhao, F.Y. Hong, K. Yang, “The influence of the elemental valence on the thermophysical properties of high entropy $(La_{0.2}Sm_{0.2}Eu_{0.2}Yb_{0.2}Y_{0.2})_2(Ce_{0.5}Zr_{0.5})_2O_7$ coatings for thermal barrier application”, *Ceram. Int.*, **50** [23] (2024) 51410–51420.
67. J. Yang, M. Zhao, L. Zhang, Z.Y. Wang, W. Pan, “Pronounced enhancement of thermal expansion coefficients of rare-earth zirconate by cerium doping”, *Scr. Mater.*, **153** (2018) 1–5.
68. X.W. Luo, S. Huang, R.Q. Huang, S. Hou, H.Y. Jin, “Phase evolution, thermophysical and mechanical properties of high-entropy $(Ce_{0.2}Nd_{0.2}Sm_{0.2}Eu_{0.2}Yb_{0.2})_2Zr_2O_7$ ceramic for advanced thermal barrier coatings”, *J. Eur. Ceram. Soc.*, **44** [4] (2024) 2452–2459.
69. K.V.G. Kutty, S. Rajagopalan, C.K. Mathews, U.V. Varadaraju, “Thermal expansion behaviour of some rare earth oxide pyrochlores”, *Mater. Res. Bull.*, **29** [7] (1994) 759–766.
70. J. Zhang, X.Y. Guo, Y. Zhang, Z. Lu, H.H. Choi, Y.G. Jung, I.S. Kim, “Mechanical properties of lanthanum zirconate-based composite thermal barrier coatings”, *Adv. Appl. Ceram.*, **118** [5] (2019) 257–263.
71. F.S. Wu, P. Wu, Y.X. Zhou, X.Y. Chong, J. Feng, “The thermo-mechanical properties and ferroelastic phase transition of $RENbO_4$ (RE = Y, La, Nd, Sm, Gd, Dy, Yb) ceramics”, *J. Am. Ceram. Soc.*, **103** [4] (2020) 2727–2740.
72. J.N. Plendl, P.J. Gielisse, “Hardness of nonmetallic solids on an atomic basis”, *Phys. Rev.*, **125** [3] (1962) 828.
73. P. Sarker, T. Harrington, C. Toher, C. Oses, M. Samiee, J.P. Maria, D.W. Brenner, K.S. Vecchio, S. Curtarolo, “High-entropy high-hardness metal carbides discovered by entropy descriptors”, *Nat. Commun.*, **9** (2018) 4980.
74. J.M. Maita, S. Rommel, J.R. Davis, H. Ryou, J.A. Wollmershauser, E.P. Gorzkowski, B.N. Feigelson, M. Aindow, S.W. Lee, “Grain size effect on the mechanical properties of nanocrystalline magnesium aluminate spinel”, *Acta Mater.*, **251** (2023) 118881.
75. Y. Zhang, L. Guo, X.X. Zhao, C.M. Wang, F.X. Ye, “Toughening effect of Yb_2O_3 stabilized ZrO_2 doped in $Gd_2Zr_2O_7$ ceramic for thermal barrier coatings”, *Mater. Sci. Eng., A*, **648** (2015) 385–391.